Konrad-Zuse-Zentrum
für Informationstechnik Berlin

Takustraße 7
D-14195 Berlin-Dahlem
Germany

GUNTER CARQUÉ, HEIKO SCHMIDT, BJORN STEVENS &
RUPERT KLEIN

Plausibility Check of an Asymptotic Column Model for Deep Convective Clouds

ZIB-Report 08-44 (November 2008)

Plausibility Check of an Asymptotic Column Model for Deep Convective Clouds

Gunter Carqué*, Heiko Schmidt**, Bjorn Stevens† &
Rupert Klein**

November 2008

*Fachbereich Mathematik & Informatik, Freie Universität Berlin
**Fachbereich Mathematik & Informatik, Freie Universität Berlin and
Konrad-Zuse-Zentrum für Informationstechnik Berlin
†Department of Atmospheric and Oceanic Sciences, University of California Los Angeles

Abstract

By use of asymptotic analysis Carqué et al. [1] derived an asymptotic column model for deep convective clouds based on the three dimensional compressible flow equations and a bulk microphysics parameterization. In the present study we check the plausibility of the reduced model equations by comparing implications of the model for the scaling of various terms in the governing equations with those extracted from large eddy simulation data based on the computational model UCLA-LES1.1. This code solves an anelastic system of equations with complete droplet based microphysics and LES closures.

We observe that the simulation data corroborate the basic assumptions of the asymptotic analysis and the main conclusions implied by the asymptotically reduced model.

The code output reflects the scales of space and time: The deep convective clouds show an anisotropic structure where the horizontal scale is considerably narrower than the vertical scale; with a period of about 20 min, from emergence to breakup, the life cycle of one particular deep convective cloud corresponds exactly to the reference time of the reduced model.

The characteristic properties of dynamics as predicted by the reduced model are also reflected in the simulation data: The horizontal flow is controlled by the pressure field; the vertical velocity develops freely independent of pressure over the depth of the convective column; the vertical velocity is directly determined by the buoyancy induced by the potential temperature deviation relative to the background stratification.

With respect to grid resolution we observe that refining the spatial step size of the equidistant computational grid from 125 m to 62.5 m does not influence the results: Even with the coarser grid the relevant physical phenomena are sufficiently resolved.

Somewhat surprisingly, the Coriolis term involving *vertical* velocity and acting on the horizontal (east-west) velocity component appears at leading order in the asymptotics. Accordingly, we expected to find a nontrivial impact of this Coriolis effect on the horizontal flow velocity components within columns of updrafts. However, switching the term on and off in subsequent simulations did not sizeably affect the results.

Contents

Notation

Latin Symbols

a	radius of the Earth
c_p	specific heat capacity at constant pressure for dry air
e_∞	triple-point vapour pressure
f	vertical Coriolis parameter
f^*	horizontal Coriolis parameter
g	acceleration of gravity
h	height
$\boldsymbol{k}$	vertical unit vector
l	length
L_{cond}	specific latent heat of condensation
p	pressure
r	mixing ratio
R	specific gas constant
S	source term
S_θ	source term due to latent heat release
t	time coordinate
u	horizontal velocity component in x-direction
v	horizontal velocity component in y-direction
$\boldsymbol{v}$	velocity vector
v_t	terminal falling velocity of rain drops
w	vertical velocity
$\boldsymbol{x}$	horizontal coordinates with respect to h_{sc}
z	vertical coordinate

Greek Symbols

γ	isentropic exponent
ε	asymptotic scaling parameter
θ	potential temperature
$\boldsymbol{\xi}$	horizontal coordinates with respect to εh_{sc}
ϱ	density
ϕ	degree of latitude
Ω	diurnal rotation frequency
$\boldsymbol{\Omega}$	Earth rotation vector
$\widehat{\boldsymbol{\Omega}}$	normalised Earth rotation vector

Dimensionless Numbers

M	Mach-Number

Mathematical Expressions and Operators

$\frac{D}{Dt}$	substantial derivative
$\exp[\cdot]$	exponential function
$\ln[\cdot]$	natural logarithm function (to the basis e)
$\sin[\cdot]$	sine function
$\cos[\cdot]$	cosine function
$\mathcal{O}(\cdot)$	Landau-Symbol
$(\cdot)^{(i)}$	i: order of the asymptotic expansion
$(\cdot)_t$	differentiation with respect to t
$(\cdot)_z$	differentiation with respect to z
∇	Nabla-Operator
$\nabla_{\boldsymbol{x}}$	Nabla-Operator regarding $\boldsymbol{x}$
$\nabla_{\boldsymbol{\xi}}$	Nabla-Operator regarding $\boldsymbol{\xi}$
$\nabla^2 = \Delta$	Laplace-Operator

Indices

c	cloud water
cloud	subdomain defining the deep convective cloud
0	surface
d	dry air
hor	horizontal
max	maximum
min	minimum
out	outside the deep convective column
r	rain water
ref	reference
sat	saturated
sc	scale
tr	tropopause
un	undersaturated
v	water vapour
ver	vertical
vs	saturated water vapour
$(\cdot)_{\shortparallel}$	horizontal part of a vector
$(\cdot)_{\perp}$	vertical part of a vector
$\overline{(\cdot)}$	averaged quantity
$\lvert(\cdot)\rvert$	absolute value of a quantity

1 Introduction

The asymptotic deep convective column model derived by Carqué et al. [1] is based on the analysis of the three dimensional compressible flow equations coupled with a bulk microphysics parameterization consisting of transport equations for the mixing ratios of the moisture species water vapour, cloud water, and rain water. This reduced model for moist atmospheric convection is characterised by an anelastic divergence constraint for the horizontal flow with a two dimensional Poisson equation for the corresponding perturbation pressure.

The aim of the present study is to compare the conclusions that can be drawn from the reduced asymptotic system of equations to simulation data based on a detailed model. For this purpose the UCLA (University of California Los Angeles) Large-Eddy Simulation Code UCLA-LES1.1 is used. This code solves an anelastic system of equations with complete droplet based microphysics. In order to confirm the plausibility of the asymptotic deep convective column model, it has to be checked whether its features are reflected in the UCLA-LES1.1 simulation data.

In this way, provided that the reduced model captures the essential mechanisms of moist convection, its solution with efficient numerical methods using moderate computational resources could then be used as a subgrid model of cloud formation and precipitation in large scale numerical weather prediction (NWP) models in the sense of superparameterization instead of a computationally intensive cloud resolving model (CRM).

So far in the superparameterization technique for each column of the coarser grid a CRM is run explicitly on a finer grid. Detailed discussions of this method are provided by Grabowski [3], [4], [5], Khairoutdinov and Randall [6] and in the review paper by Randall et al. [11]. Recent publications on this topic are provided by Majda [9] and Majda and Xing [10]. The comparison between superparameterization and conventional subgrid models of convective clouds for the NCAR (National Center for Atmospheric Research) climate model by Khairoutdinov et al. [7] shows that the superparameterization technique is very computing time consuming at present and can therefore not be applied to weather forecast models right now. Perhaps the asymptotically reduced model investigated in this study might be used for superparameterization in operational weather forecast models in the future.

In section 2 we show the equations of the asymptotically reduced model from [1] for saturated and undersaturated conditions. Section 3 presents the model equations, the parameterizations and the numerical algorithm implemented in UCLA-LES1.1. This section also describes the initial and boundary

conditions used to initialise deep convection and illustrates the characteristics of the observed deep convective clouds. In section 4 we explain how the asymptotic perturbation quantities are extracted from the code-output. In order to get to know the behaviour of the code, we also study its representation of hydrostatics and the compliance with the divergence constraint in this section. Section 5 provides the detailed discussion of the correlations between the asymptotic unknowns themselves and between the terms in the asymptotic vertical momentum balance. This section also discusses the simulation with higher spatial resolution and the simulation with the horizontal Coriolis parameter. In section 6 we draw the conclusions of the comparison between the asymptotically reduced model and the UCLA-LES1.1 data.

2 Summary of the asymptotic model equations

Before we embark on the plausibility check, here we show the equations of the asymptotically reduced model from [1] for saturated and undersaturated conditions.

In the saturated air regime the final system of equations contains the unknown variables $p^{(6)}$, $\theta^{(4)}$, $\boldsymbol{v}_{\shortparallel}^{(1)}$ and $w^{(0)}$. With these quantities the coupled mixing ratios of cloud and rain water can be determined. The equations read as follows:

Saturated Air

Mass Balance

$$\varrho^{(0)} \nabla_{\boldsymbol{\xi}} \cdot \boldsymbol{v}_{\shortparallel}^{(1)} + (\varrho^{(0)} w^{(0)})_z = 0,$$

Horizontal Momentum Balance

$$\boldsymbol{v}_{\shortparallel t}^{(1)} + (\boldsymbol{v}_{\shortparallel}^{(1)} \cdot \nabla_{\boldsymbol{\xi}}) \boldsymbol{v}_{\shortparallel}^{(1)} + w^{(0)} \boldsymbol{v}_{\shortparallel z}^{(1)} + (w^{(0)} \widehat{\boldsymbol{\Omega}}_{\shortparallel} \times \boldsymbol{k}) + \frac{1}{\varrho^{(0)}} \nabla_{\boldsymbol{\xi}} p^{(6)} = 0,$$

Vertical Momentum Balance

$$w_t^{(0)} + \boldsymbol{v}_{\shortparallel}^{(1)} \cdot \nabla_{\boldsymbol{\xi}} w^{(0)} + w^{(0)} w_z^{(0)} = \theta^{(4)} - \theta_{\text{out}}^{(4)},$$

Transport Equation for the Potential Temperature

$$\theta_t^{(4)} + \boldsymbol{v}_{\shortparallel}^{(1)} \cdot \nabla_{\boldsymbol{\xi}} \theta^{(4)} + w^{(0)} \theta_z^{(4)} = w^{(0)} (\theta_z^{(4)})_{\text{out}},$$

Transport Equation for the Cloud Water Mixing Ratio

$$K_{vc} w^{(0)} r_{vs}{}_z^{(0)} + C_{cr,1} r_c^{(0)} r_r^{(0)} = 0,$$

Transport Equation for the Rain Water Mixing Ratio

$$r_{rt}^{(0)} + \boldsymbol{v}_{\shortparallel}^{(1)} \cdot \nabla_{\boldsymbol{\xi}} r_r^{(0)} + w^{(0)} r_{rz}^{(0)} - V_r \frac{1}{\varrho^{(0)}} (\varrho^{(0)\,\frac{1}{2}} r_r^{(0)})_z - C_{cr,2} r_c^{(0)} r_r^{(0)} = 0.$$

The reduced system for the undersaturated air regime consists of the following equations with $p^{(6)}$, $r_v^{(0)}$, $r_r^{(0)}$, $\boldsymbol{v}_{\shortparallel}^{(1)}$ and $w^{(0)}$ as unknown variables:

Under-Saturated Air

Mass Balance

$$\varrho^{(0)} \nabla_{\boldsymbol{\xi}} \cdot \boldsymbol{v}_{\shortparallel}^{(1)} + (\varrho^{(0)} w^{(0)})_z = 0,$$

Horizontal Momentum Balance

$$\boldsymbol{v}_{\shortparallel t}^{(1)} + (\boldsymbol{v}_{\shortparallel}^{(1)} \cdot \nabla_{\boldsymbol{\xi}})\boldsymbol{v}_{\shortparallel}^{(1)} + w^{(0)}\boldsymbol{v}_{\shortparallel z}^{(1)} + (w^{(0)}\widehat{\boldsymbol{\Omega}}_{\shortparallel} \times \boldsymbol{k}) + \frac{1}{\varrho^{(0)}}\nabla_{\boldsymbol{\xi}} p^{(6)} = 0,$$

Transport Equation for the Potential Temperature

$$w^{(0)}\theta_z^{(2)} = -\Gamma L E_r^{(0)},$$

Transport Equation for the Water Vapour Mixing Ratio

$$r_{v\,t}^{(0)} + \boldsymbol{v}_{\shortparallel}^{(1)} \cdot \nabla_{\boldsymbol{\xi}} r_v^{(0)} + w^{(0)} r_{v\,z}^{(0)} = E_r^{(0)},$$

Transport Equation for the Rain Water Mixing Ratio

$$r_{r\,t}^{(0)} + \boldsymbol{v}_{\shortparallel}^{(1)} \cdot \nabla_{\boldsymbol{\xi}} r_r^{(0)} + w^{(0)} r_{r\,z}^{(0)} - V\frac{1}{\varrho^{(0)}}\left((\varrho^{(0)})^{\frac{1}{2}} r_r^{(0)}\right)_z = -E_r^{(0)}.$$

The above equations originate from the asymptotic analysis of a convective system on the horizontal bulk micro scale of 1 km for the moist atmosphere. It is characterised by the deep convective vertical scale of 10 km and the corresponding convective time scale of 20 min.

The resulting model shows some special features:

- The continuity equation provides an anelastic divergence constraint for the horizontal flow. The perturbation pressure representing the corresponding Lagrange multiplyer obeys a two dimensional Poisson equation.
- The horizontal momentum balance contains the product of the leading-order vertical velocity and the horizontal Coriolis parameter, a term that is usually neglected in meteorological applications.
- In the saturated column, the vertical velocity is directly determined by the potential temperature deviation between inside the column and outside, which is a conserved quantity. In the undersaturated regime, the vertical velocity depends on the leading order evaporation rate which in turn is constituted by the saturation deficit and the amount of rain water present.

For a detailed discussion of the model's properties we refer the reader to [1].

3 The UCLA Large-Eddy Simulation Code

3.1 Survey of UCLA-LES1.1

UCLA-LES1.1 [14] is a large eddy simulation (LES) model for meteorological studies. In contrast to Reynolds averaged Navier Stokes (RANS) models, where

the underlying set of equations is ensemble filtered, in LES the filter operation acts spatially. In this section the filtered quantities will be dentoted by an overbar. Whereas in RANS only the turbulent eddies of integral scales are resolved, in LES also smaller eddies with length scales down to the filter induced cut-off are taken into account.

UCLA-LES1.1 is configured to solve a spatially filtered system of anelastic equations on the f-plane in three space dimensions x, y, z and time t. It is written in F90/95, and is parallelised using a one-dimensional decomposition and MPI. The grid is doubly periodic in the horizontal (x-y) and bounded in the vertical, z. The vertical is spanned by a stretchable grid, the horizontal by uniform squares. Prognostic variables include the three components of the wind ($u_i \equiv \{u, v, w\}$), the liquid-water potential temperature, θ_l, the total-water mixing ratio, q_t, and an arbitrary number of scalars, ϕ_m, in support of microphysical processes, more sophisticated sub-grid models, or studies of tracer transport or chemical processes. Time-stepping of the momentum equations is by the leap-frog method. Scalars are advanced using a forward-in-time integration scheme. Scalar advection is based on a directional-split monotone up winding method while momentum advection uses directionally-split fourth-order centered differences.

3.1.1 Model Equations

The form of the equations solved by the model are (in tensor notation) as follows:

$$\frac{\partial \bar{u}_i}{\partial t} = -\bar{u}_j \frac{\partial \bar{u}_i}{\partial x_j} - c_p \Theta_0 \frac{\partial \bar{\pi}}{\partial x_i} + \frac{g\bar{\theta}_v''}{\theta_0}\delta_{i3} + f_k(\bar{u}_j - u_{j,g})\epsilon_{ijk} + \frac{1}{\rho_0}\frac{\partial(\rho_0 \tau_{ij})}{\partial x_j} \quad (1)$$

$$\frac{\partial \bar{\phi}}{\partial t} = -\bar{u}_j \frac{\partial \bar{\phi}}{\partial x_j} + \frac{1}{\rho_0}\frac{\partial(\rho_0 \gamma_{\phi j})}{\partial x_j} + \frac{\partial F_\phi}{\partial x_j}\delta_{j3}, \quad (2)$$

subject to the anelastic continuity equation

$$\frac{\partial(\rho_0 u_i)}{\partial x_i} = 0 \quad (3)$$

and a constitutive equation which we take to be the ideal gas law for a perfect mixture:

$$\theta_v = \theta\left(1 + (R_v/R_d - 1)q_t - (R_v/R_d)q_l\right). \quad (4)$$

In the above $\tilde{\pi} = (\tilde{p}/p_{00})^{R/c_p}$ is the dynamic pressure perturbation. F_ϕ denotes a flux whose divergence contributes to the evolution of ϕ (for instance radiation in the case of $\phi = \theta_l$), $f_k = \{0, 0, f\}$ is the Coriolis parameter, $u_{j,g}$ is the geostrophic wind, and

$$\tau_{ij} \equiv \overline{u_i u_j} - \bar{u}_i \bar{u}_j \quad \text{and} \quad \gamma_{\phi j} \equiv \overline{\phi u_j} - \bar{\phi}\bar{u}_j \quad (5)$$

denote the sub-grid fluxes. In (2) ϕ denotes an arbitrary scalar. Depending on the level of microphysical complexity this can include θ_l and q_t or an arbitrary number of additional variables, for instance to represent microphysical habits or categories. The symbols δ_{jk} and ϵ_{ijk} denote the Kronecker-delta and Levi-Civita symbol respectively.

The anelastic approximation solves for perturbations about a hydrostatic basic state of fixed potential temperature, i.e.,

$$\frac{d\pi_0}{dz} = -\frac{g}{c_p\Theta_0}, \tag{6}$$

where subscript 0 denotes a basic state value, which depends only on z (Θ_0 being constant). In (1) $\bar{\theta}_v''$ denotes the deviation of θ_v from its horizontal average (rather than from the basic-state). This ensures that no mean vertical accelerations arise. For consistency we introduce a second pressure, π_1 :

$$\frac{d}{dz}(\pi_0 + \pi_1) = -\frac{g}{c_p\bar{\theta}_v}, \tag{7}$$

that contains the contribution of deviations from the Θ_0 reference state to the pressure. This pressure depends on time, and is updated in the code by finding the pressure that balances the mean accelerations, such that

$$\frac{d\pi_1}{dz} = \Theta_0\overline{w}, \tag{8}$$

with $\pi_1(z = 0)$ fixed at its initial value.

The model represents the First Law of thermodynamics by (2) with $\phi = \theta_l$. Where we define θ_l as:

$$\theta_l = T\pi \exp\left(-\frac{q_l L_v}{c_p T}\right) \tag{9}$$

Hence the model satisfies an approximate form of the First Law, but one generally consistent with the overall level of approximation. In the above L_v, R_d, R_v, c_p and p_{00} are thermodynamic parameters which adopt standard values given in the code documentation [14]. Finally, g is the gravitational acceleration.

The continuity equation (3) yields $\tilde{\pi}$ through the inversion of the Poisson equation

$$\frac{\partial}{\partial x_i}\left(\rho_0\frac{\partial\tilde{\pi}}{\partial x_i}\right) = \frac{1}{c_p\Theta_0}\left[\frac{\partial}{\partial x_i}\left(-\rho_0\bar{u}_j\frac{\partial\bar{u}_i}{\partial x_j} + \frac{\rho_0 g\bar{\theta}_v''}{\theta_0}\delta_{i3} + \rho_0 f_k(\bar{u}_j - u_{jg})\epsilon_{ijk} + \frac{\partial(\rho_0\tau_{ij})}{\partial x_j}\right)\right]. \tag{10}$$

3.1.2 Parameterizations

Since the basic fluid equations have been spatially filtered, the net effect of the subgrid or better subfilter scales has to be given. This is normally called parameterization or closure. Note that this process might be very crucial depending on the origin of the investigated problem. For flows dominated by large eddies one can argue that the results are not too sensitive to a variation of parameterization, while for small scale dominated flows the closure is the most crucial point. In the code the following closures are used.

Turbulence

The sub-grid fluxes τ_{ij} and $\gamma_{\phi j}$ are not known explicitly and thus must be modeled. This constitutes the model closure. The basic or default form of the closure makes use of the Smagorinsky model, wherein

$$\tau_{ij} = -\rho_0 K_m D_{ij} \quad \text{and} \quad \gamma_{\phi j} = -\frac{K_m}{Pr}\frac{\partial \bar{\phi}}{\partial x_j}, \tag{11}$$

where

$$D_{ij} = \frac{\partial \bar{u}_i}{\partial x_j} + \frac{\partial \bar{u}_j}{\partial x_i}$$

is the resolved deformation, K_m is the eddy viscosity, and Pr is an eddy Prandtl number. The Smagorinsky model calculates the eddy viscosity as

$$K_m = (C_s \ell)^2 S \sqrt{1 - \frac{Ri}{Pr}} \quad \text{where} \quad Ri = \frac{N^2}{S^2} \tag{12}$$

and

$$S^2 \equiv \frac{\partial \bar{u}_i}{\partial x_j} D_{ij} \quad \text{and} \quad N^2 = \frac{g}{\Theta_0}\frac{\partial \bar{\theta}_v}{\partial z}. \tag{13}$$

In the above C_s is the Smagorinsky constant and takes values near 0.2, and

$$\ell^{-2} = (\Delta x \Delta y \Delta z)^{-2/3} + (z\kappa/C_s)^{-2},$$

where $\kappa = 0.35$ is the von Kármán constant in the model. The geometric averaging between a grid scale and a length scale proportional to the height above the surface allows $K_m/(u_* z)$ to approach κ in the neutral surface layer (the log-law). Other options (not used in the present study) include Lagrangian averaged scale-dependent and scale-independent models, the Deardorff-Lilly sub-grid turbulence kinetic energy (TKE) model, and for scalars the option of having all the dissipation carried by the numerics.

Cloud microphysics

A variety of microphysical complexity can be included into UCLA-LES1.1. In the standard distribution a warm-rain microphysical scheme (level 3, type 2) is implemented following the work of Seifert and Beheng [13]. In this scheme cloud droplets are assumed to be in equilibrium with a fixed (specified) concentration. Cloud, or rain, drops defined as liquid condensate with appreciable fall velocities are allowed to evolve under the action of the ambient flow and microphysical processes (auto-conversion, accretion, self-collection, sedimentation). The representation of these processes leads to the inclusion of two additional prognostic equations, one for rain mass the other for rain concentration.

A saturation adjustment scheme (level 2, type 0) is also implemented in the model. This scheme has no rain category and diagnoses cloud drop mass concentrations by assuming homogeneity on the grid-scale and equilibrium thermodynamics. Sedimentation of cloud droplets can be implemented as a source term in the model (level=2, type=1). For details we refer the reader to [14].

Boundary conditions and surface fluxes
To enforce the boundary conditions, the model can either implement free slip or no-slip boundary conditions on the grid-scale tangential velocities, with free-slip being the default. These grid-scale quantities do, however, feel accelerations, or tendencies as a result of sub-grid scale fluxes which are parameterized. The model supports different methodologies for specifying the sub-grid fluxes at the lower boundary. They can be prescribed, calculated based on prescribed gradients, or prescribed surface properties. For the latter two similarity functions are chosen to relate the fluxes at the surface to the grid-scale gradients there. For details we refer the reader again to [14].

3.1.3 Numerical Algorithm

In the following we summarise the numerical procedure used in UCLA-LES1.1.

Time-stepping
The model uses a hybrid time-stepping strategy. At the top of the timestep

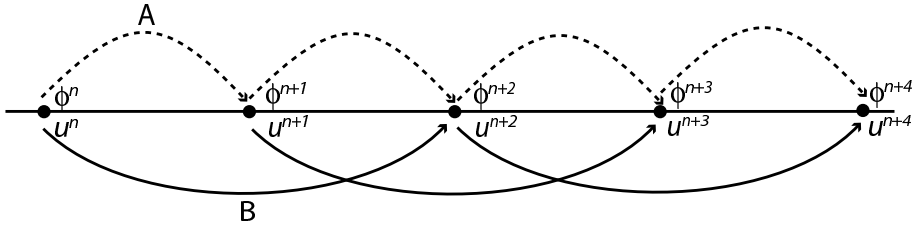

Figure 1: Schematic depiction of the model time-step.

velocities are given at time level n and $n+1$ and scalars are given at time level n.

The scalars are then marched forward using an Euler forward step to time-level $n+1$. Velocities from time-level n are then taken forward using a leapfrog step to time-level $n+2$ which concludes a single step. On a timestep tendencies are accumulated in a tendency array and then applied at the end of the step. An exception to this are the subgrid fluxes, which involve a diffusion operation. The vertical component of this operation is solved semi-implicitly which requires a sparse matrix solve (a tri-diagnonal solver). The new velocity is then differenced with the old velocity to define an effective forward tendency which is accumulated like the other forcings in the tendency array. Mathematically, if the time-level is indicated by a superscript, then

$$\left(\frac{\partial \phi}{\partial t}\right)_{sgs} = \frac{\tilde{\phi}^{n+1} - \phi^n}{\Delta t} \quad \text{where} \quad \tilde{\phi}^{n+1} = \phi^n + \Delta t \frac{\partial}{\partial z}\left(K^n \frac{\partial \tilde{\phi}^{n+1}}{\partial z}\right), \tag{14}$$

where $K \equiv K_m/Pr$ is the eddy diffusivity. Another exception is the pressure gradient term which is solved so as to ensure that the discretized version of

$$\frac{\partial}{\partial x_i}\left(\rho_0 \bar{u}_i\right) = 0 \tag{15}$$

is satisfied to machine precision.

Computational Grid

The model uses the Arakawa-C grid, which means that $u(k,i,j)$ lies a distance of

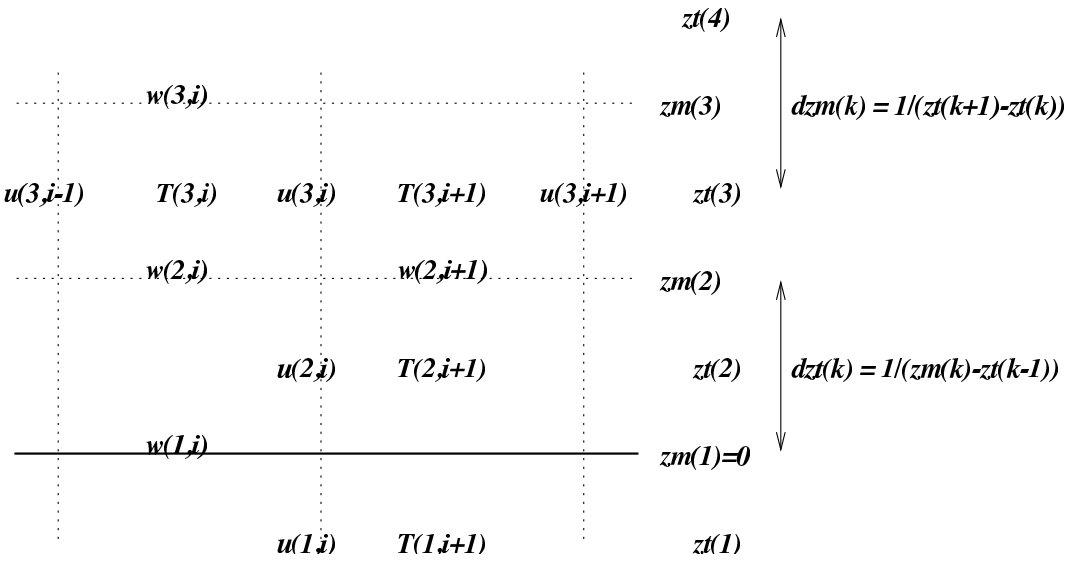

Figure 2: Schematic depiction of the model grid and where variables locate on it.

$\frac{\Delta x}{2}$ to the right of $\theta_l(k,i,j)$. To state this more generally, velocities are staggered half a grid point up-grid (in the direction of the specific velocity component)

of the thermodynamic and pressure points. Also note that the grid indexing has the z dimension first. This k, i, j indexing is chosen in realisation of the fact that many of the operations in the model are done column-wise. The grid configuration, and some height variables that are commonly used in the code (i.e., *zm, zt, dzm,* and *zt*) are illustrated in a schematic drawing in figure 2.

Pressure Solver
Pressure is solved by a fractional step method so as to ensure that the velocities at the end of the timestep satisfy (3) to machine accuracy. The solver takes advantage of the periodicity in the horizontal to use 2-D FFTs to transform the Poisson-equation to a second order ODE in the vertical. Schematically

$$\frac{\partial^2 \pi}{\partial x_i^2} \longrightarrow (l^2 + m^2)\frac{d^2\pi}{dz^2}, \tag{16}$$

where l and m denote the horizontal wave-numbers. The resultant ODE is then solved using a tri-diagnonal solver.

3.2 Setting of the simulations

In our simulations the extent of the computational domain amounts to 32 km in the horizontal and 15 km in the vertical. This volume is discretised by an equidistant grid with a spacing of 125 m. Thus the resolution results in 256 x 256 x 120, so almost 8 million grid points. At the beginning of the computation the temporal step size is 2.0 s which is adaptively reduced to values between 1.0 s and 1.5 s during the run so that the CFL number always stays smaller than 0.8. A time period of 21600 s $\widehat{=}$ 6 h is simulated. The UCLA-LES-Code is run in parallel on 32 processors and performs about 16800 time steps in a total of about 20 h.

The parallel high performance computing is carried out on the IBM p655 Cluster with a total of 240 IBM Power4 CPU at the Potsdam Institute for Climate Impact Research (PIK). The cluster is run under the AIX5 operating system and uses the IBM Load Leveler batch queuing system. For more information, see [18].

3.2.1 Basic state

In order to initialise deep convective events, constant surface fluxes of sensible and latent heat are prescribed. The potential temperature θ and relative humidity U profiles for the initial sounding are defined following the paper by Weisman and Klemp [20] also used by Seifert [12] to simulate deep convective clouds:

$$\theta(z) = \begin{cases} \theta_0 + (\theta_{tr} - \theta_0)\left(\frac{z}{z_{tr}}\right)^{(5/4)} & : \quad z \leq z_{tr} \\ \theta_{tr} \exp\left[\frac{g}{c_p T_{tr}}(z - z_{tr})\right] & : \quad z > z_{tr} \end{cases} \tag{17}$$

$$U(z) = \begin{cases} U_{max} - (U_{max} - U_{min})\left(\frac{z}{z_{tr}}\right)^{(5/4)} & : \quad z \leq z_{tr} \\ U_{min} & : \quad z > z_{tr} \end{cases} \tag{18}$$

In the above equations $z_{tr} = 12\,\mathrm{km}$, $\theta_{tr} = 343\,\mathrm{K}$ and $T_{tr} = 213\,\mathrm{K}$ represent the height, potential temperature and actual temperature, respectively, at the tropopause, $\theta_0 = 300\,\mathrm{K}$ is the surface potential temperature. Relative humidity takes values between $U_{min} = 0.25$ and $U_{max} = 1.00$.

Preprocessing is done using the numerical computing environment MATLAB R2007a from The MathWorks, Inc. [16]. The potential temperature and relative humidity profiles are visualised in figures 3 and 4.

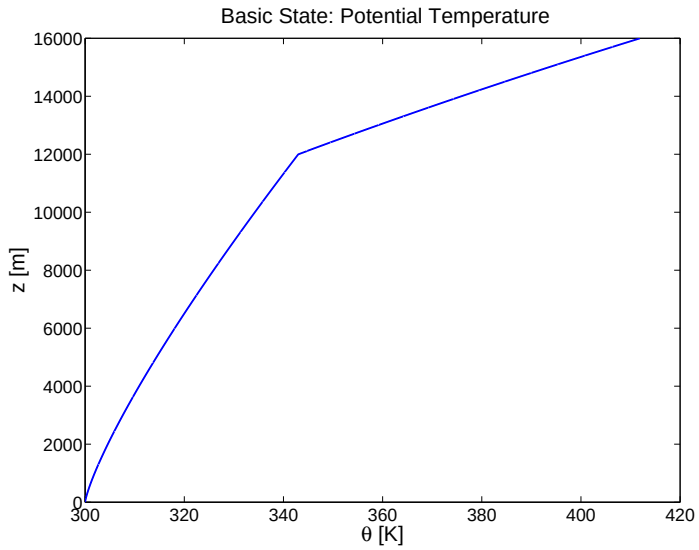

Figure 3: Potential temperature of the initial sounding.

When converting the relative humidity into the water vapour mixing ratio distribution needed for the code's input file a maximum mixing ratio of $12\,\mathrm{g\,kg^{-1}}$ near the ground is fixed to describe the well mixed boundary layer. Even though a higher mixing ratio in the bundary layer moves the lifting condensation level upwards computations by the authors showed no influence on the location of the cloud top. Figure 5 shows the water vapour mixing ratio profile of the basic state.

As for the simulations discussed in this work the atmosphere is at rest, i.e. there is no wind profile prescribed, $u = v = 0\,\mathrm{ms^{-1}}$.

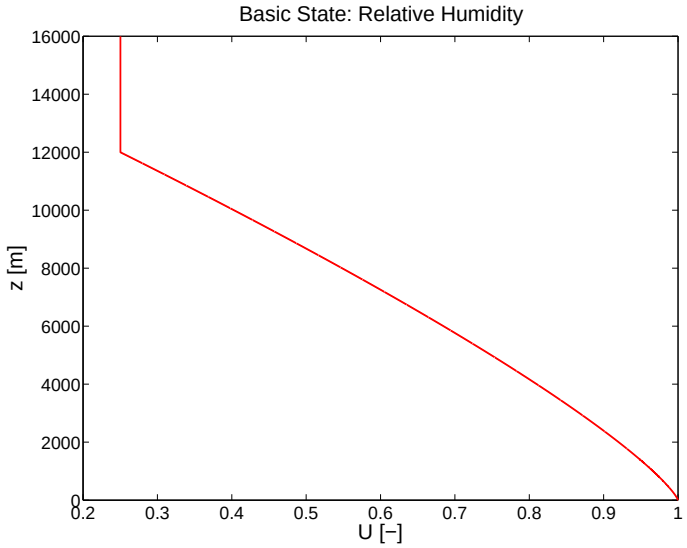

Figure 4: Relative humidity of the initial sounding.

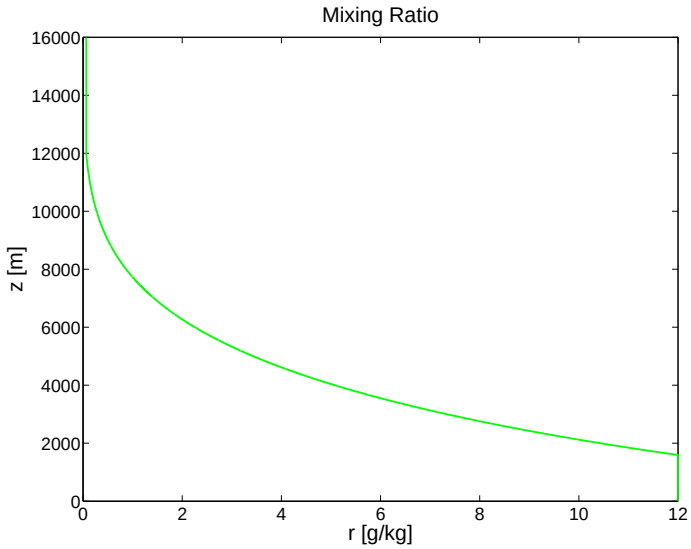

Figure 5: Water vapour mixing ratio of the initial sounding.

3.2.2 Reference run

After three hours of simulated time the first deep convective columns can be observed. All of them are characterised by the spatial anisotropic structure that is consistent with the scaling chosen for the asymptotic analysis.

In the following we illustrate this with a column whose dimensions and velocity values are representative for the clouds occuring throughout the computation. This column around the local maximum of vertical velocity after three hours and fifty minutes of simulated time provides the basis for the detailed discussion in section 5.

Postprocessing of the netCDF[1]-data is done using the NCAR Command Language (NCL) from the National Center for Atmospheric Research (NCAR) [17]. Figure 6 shows the contour plot of vertical velocity for the region of that specific column on a vertical slice through the maximum of vertical velocity.
We observe an isotropic region around the maximum vertical velocity of $21\,\mathrm{ms}^{-1}$ reached at a height of about 5 km. This region is characterised by steep spatial (vertical and horizontal) gradients of vertical velocity. In contrast, the vertical velocity varies much more slowly with height through the lower part of the column.

To visualise the depth of the convective towers, figure 7 shows the corresponding vertical slice of the whole domain.

Figure 8 presents the contour plot of vertical velocity in a horizontal slice through the maximum of vertical velocity for the deep convective cloud from figure 6.
We observe the nearly cylindrical cross section of the tower and the nearly axisymmetric velocity distribution with steep spatial gradients inside the column. Outside the column the region of compensating downward motion with negative vertical velocity can be identified.

In figure 9 the corresponding horizontal slice through the whole domain is displayed. It illustrates the distribution of deep convective events over the computational area at one particular instance in time.

To visualise the horizontal flow, we plot in figure 10 the streamlines for different horizontal slices through the deep convective column, the background colour indicates the absolute value of horizontal velocities.
The first three graphs show cross sections at 375 m, 250 m and 125 m below

[1] netCDF (network Common Data Form) is a set of software libraries and machine-independent data formats that support the creation, access, and sharing of array-oriented scientific data [19].

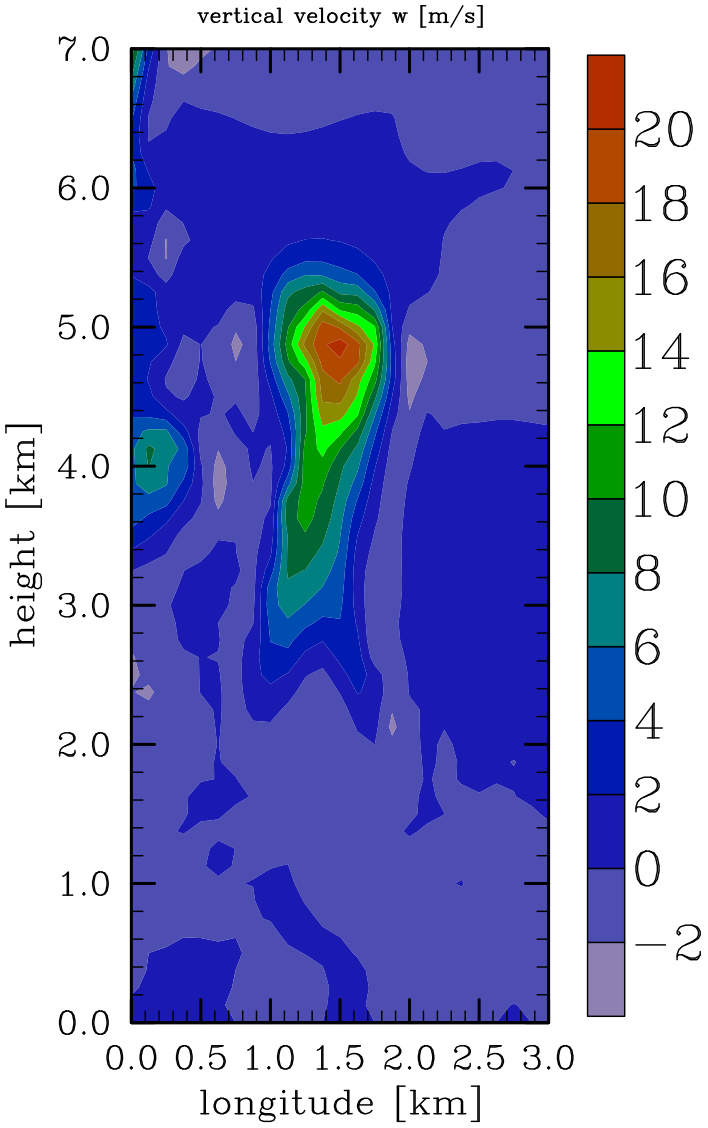

Figure 6: Vertical velocity of a vertical slice through the deep convective column.

the maximum vertical velocity, respectively, illustrating the air flow that moves towards the cloud centre to compensate the upwards mass transport. The following three graphs represent cross sections at 125 m, 250 m and 375 m above the maximum vertical velocity, respectively, where the air is displaced outwards. The absolute value of horizontal velocities continuously rises over this part of the cloud.

The vertical slice in figure 11 displays the usual surface bubbles of warm and moist air building due to the prescribed surface fluxes of sensible and latent heat.

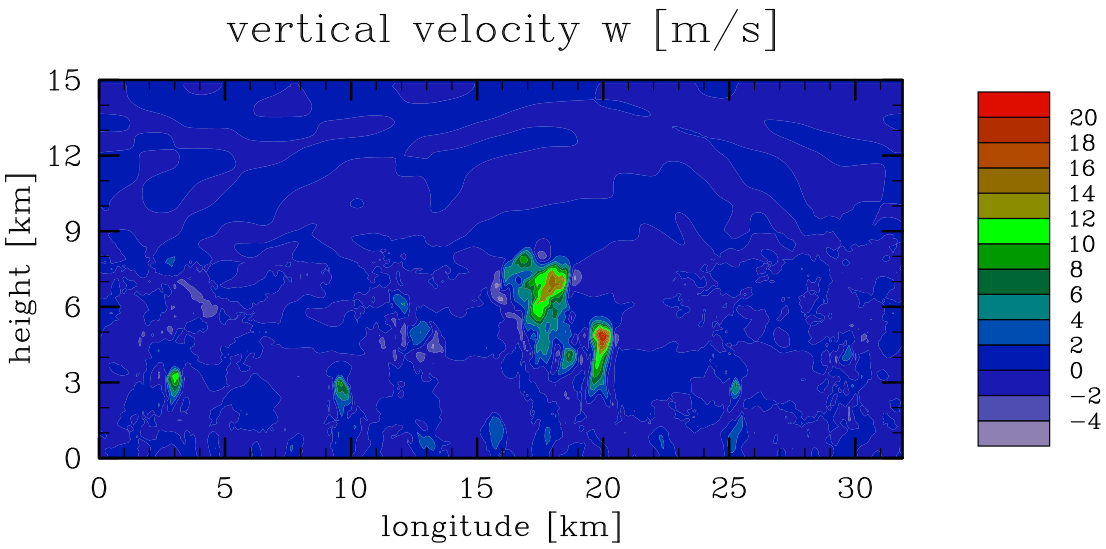

Figure 7: Vertical velocity of a vertical slice through the whole domain.

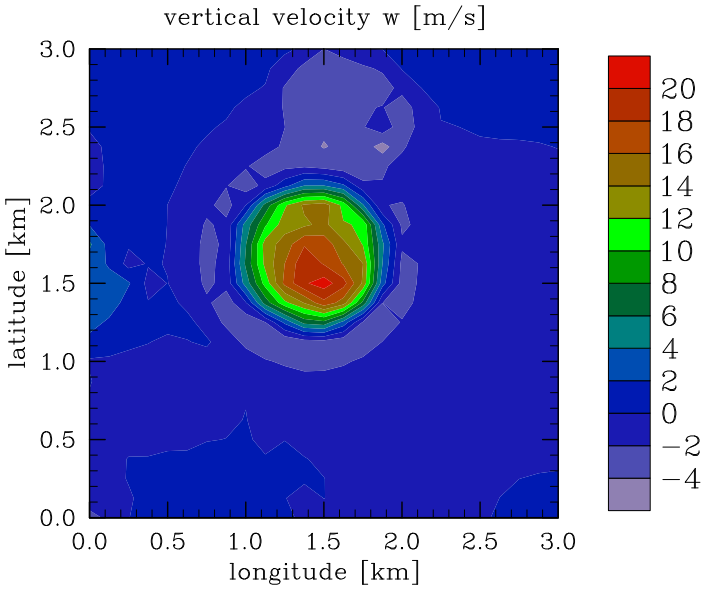

Figure 8: Vertical velocity of a horizontal slice through the deep convective column.

Figures 12 and 13 describe the entire life cycle of the deep convective column. The graphs in both figures are to be read row by row, each with the sequence from the left to the right. The colour code changes from graph to graph.
In both figures the graphs follow each other in one minute intervals. The passage from figure 12 to 13 also accounts for a one minute interval.

Thus from emergence to breakup the life cycle of the deep convective cloud covers a period of 18 min. This is in perfect accordance to the reference time of

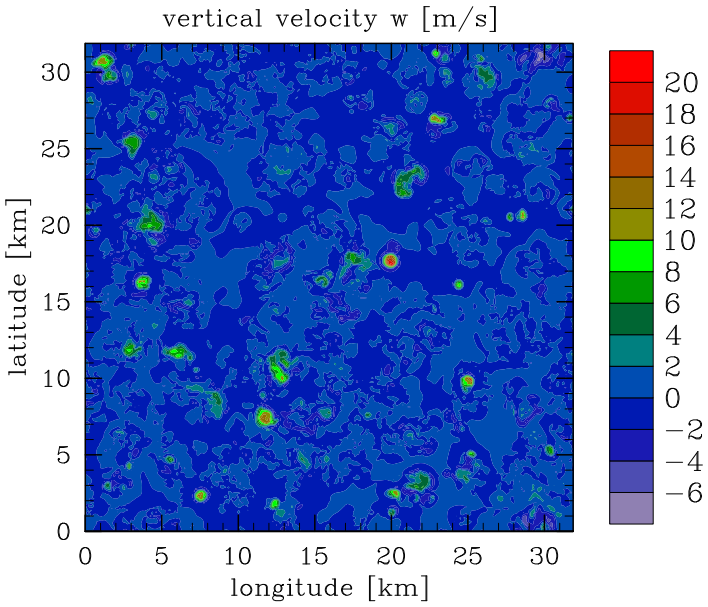

Figure 9: Vertical velocity of a horizontal slice through the whole domain.

about 20 min the reduced asymptotic model is based on.

In figure 12 we see that at some point the bubble raises and loses contact with the boundary layer. It then rises independently of the surface fluxes, i.e. it is not continously fed from below but by the latent heat release due to condensation. The first picture of the third row is the same as figure 6. It represents the moment of the maximum vertical velocity in the tower.

In figure 13 negative values of vertical velocitity do not only occur at the edges of the cloud where air moves downwards for continuity reasons. We also observe regions of negative vertical velocity in the inner of the column indicating falling rain drops.

In order to demonstrate that the region of positive vertical velocity perfectly correlates with the region of positive cloud water content, figures 14 and 15 present the contour plots of cloud water mixing ratio on the vertical and horizontal slices through the tower, respectively.

Figure16 represents a three dimensional snapshot of the whole computational domain at an arbitrary moment during the last three hours of simulated time.[2] White colour denotes the cloud water mixing ratio, dark blue colour stands

[2]3D-graphics and movies are produced using the visualisation and graphical analysis tool VISIT from the Lawrence Livermore National Laboratory (LLNL) [15].

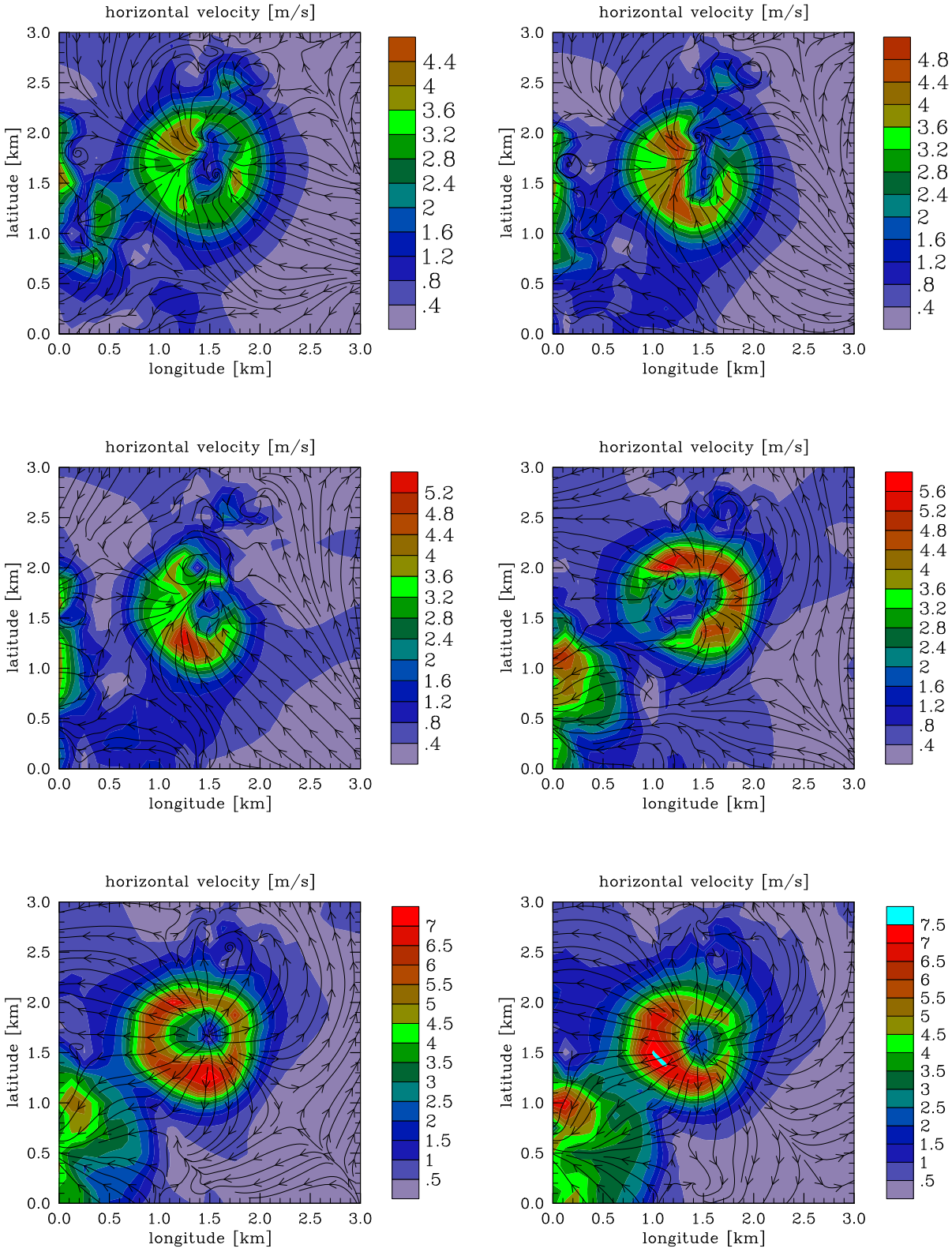

Figure 10: Streamlines and absolute value of horizontal velocities for cross sections of the cloud at different height levels. First row: 375 m below and 250 m below w_{max}. Second row: 125 m below and 125 m above w_{max}. Third row: 250 m above and 375 m above w_{max}.

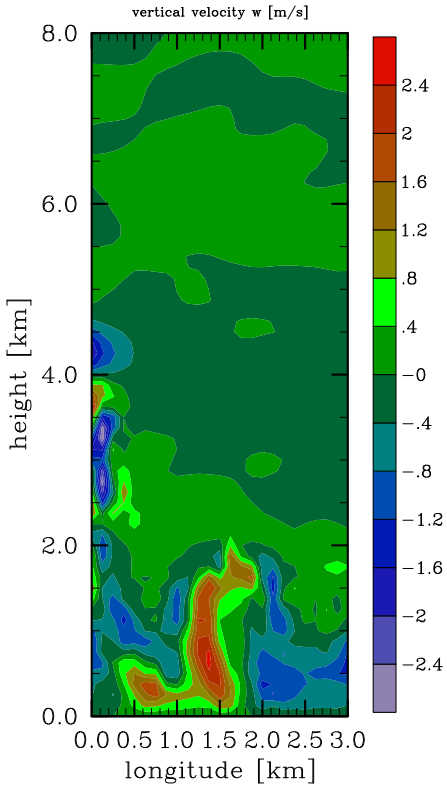

Figure 11: Bubbles of warm and moist air near the surface.

for the rain water mixing ratio. Displayed are values greater than or equal to $2\,\mathrm{gkg}^{-1}$. The maximum values amount to $8\,\mathrm{gkg}^{-1}$ for both quantities at that particular point in time. In grey coloured regions dark blue rain water shows through the white cloud water.

This snapshot illustrates impressively the transition from cloud water to rain water. Moreover it communicates a good impression of the distribution of deep convective towers over the computational domain. Those are indeed very concentrated and separated from each other which is in agreement with the basic assumptions of the theory.

In order to obtain an overview over several single deep convective events, table 1 summarises characteristic velocities and dimensions of clouds occuring throughout the last three hours of simulated time.

For each point in time the cloud around the local maximum of vertical velocity is listed. Their locations in the computational area differ completlely one from the other. Table 1 provides the maximum velocities w_{max}, u_{max}, v_{max}, the height of the maximum vertical velocity $h_{w_{max}}$ and the extensions of the deep convective cloud $\Delta z_{\mathrm{cloud}}$, $\Delta x_{\mathrm{cloud}}$, $\Delta y_{\mathrm{cloud}}$. The last row yields the averaged values of the

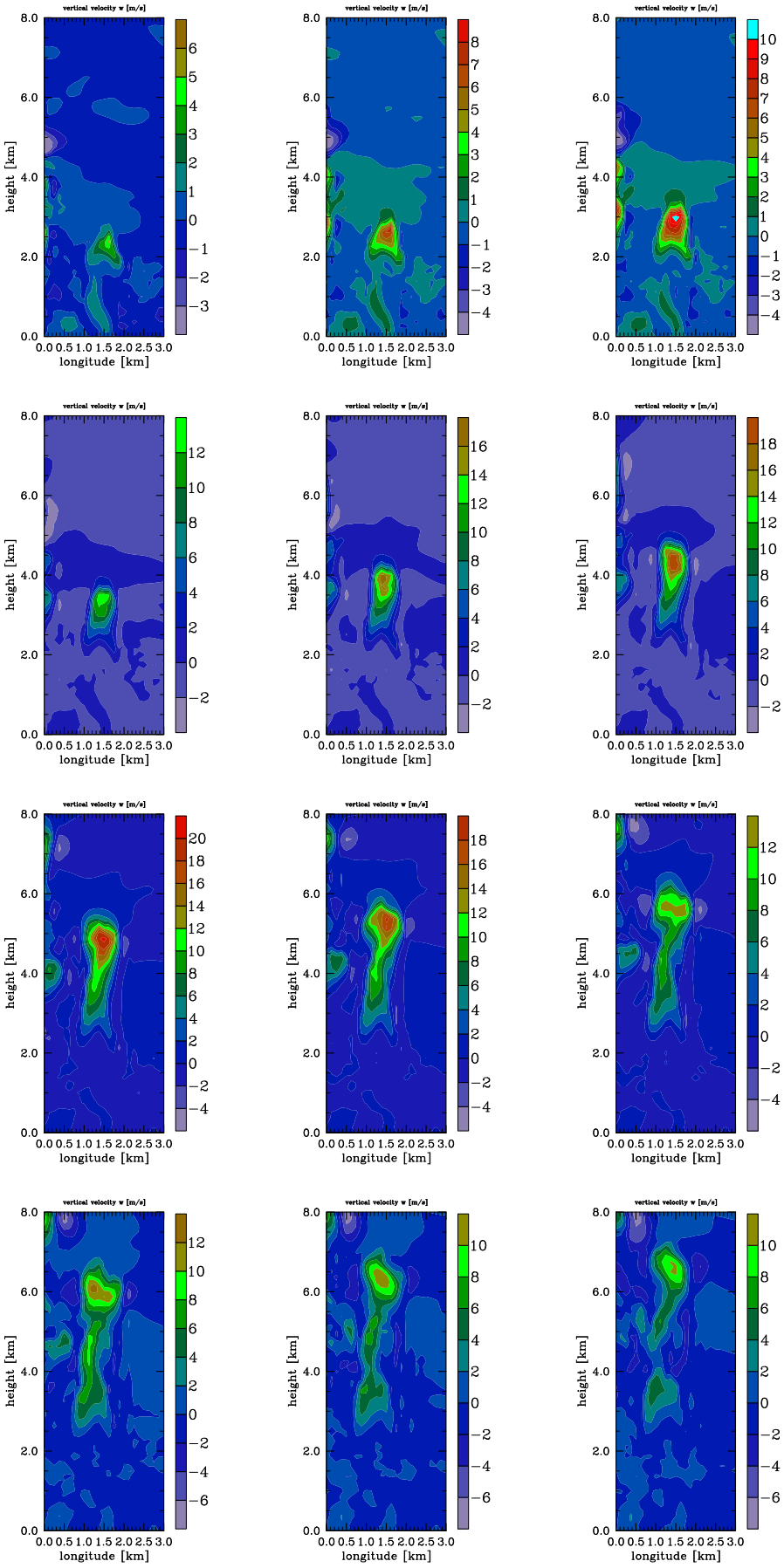

Figure 12: Part of the cloud life cycle without rain.

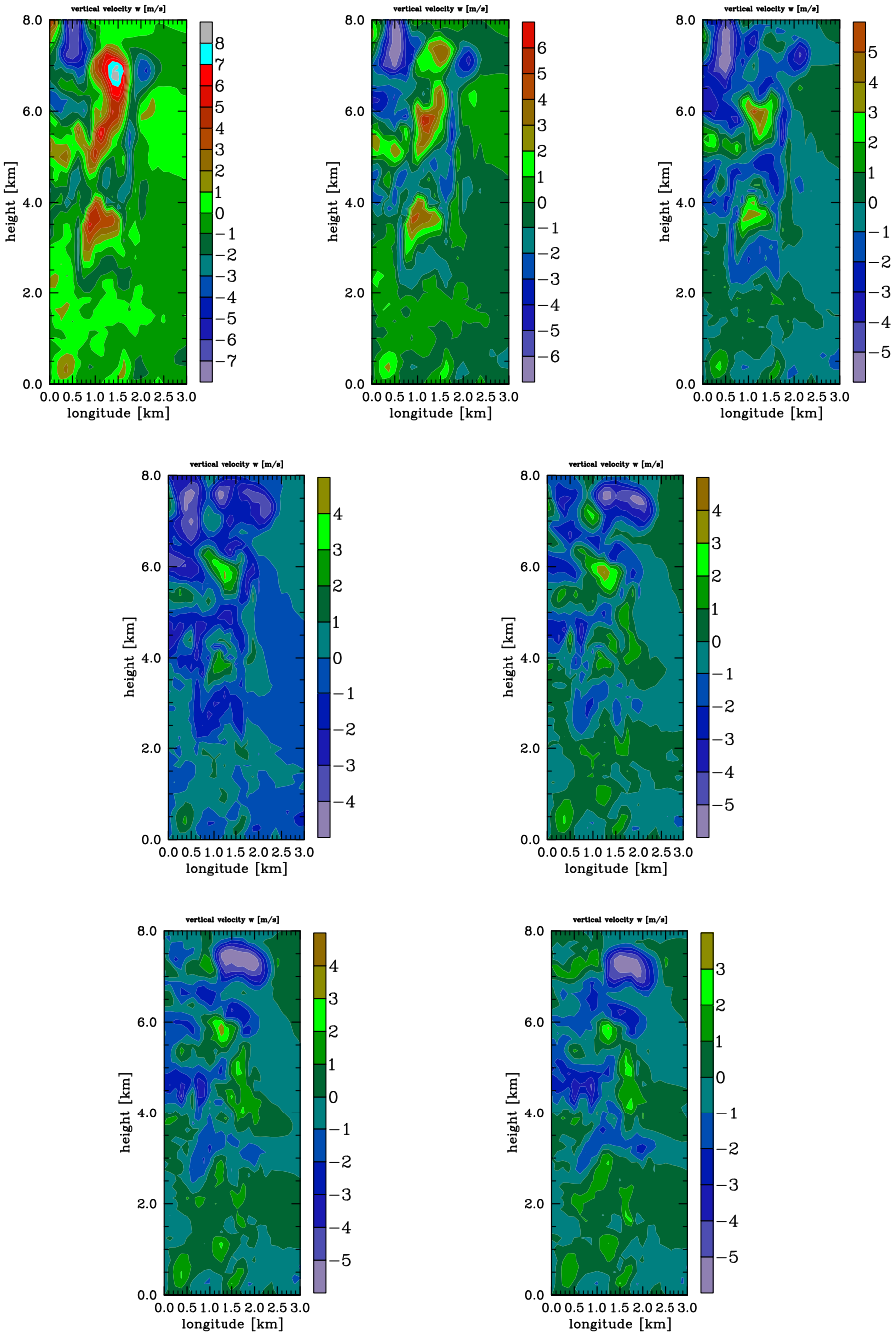

Figure 13: Part of the cloud life cycle with rain.

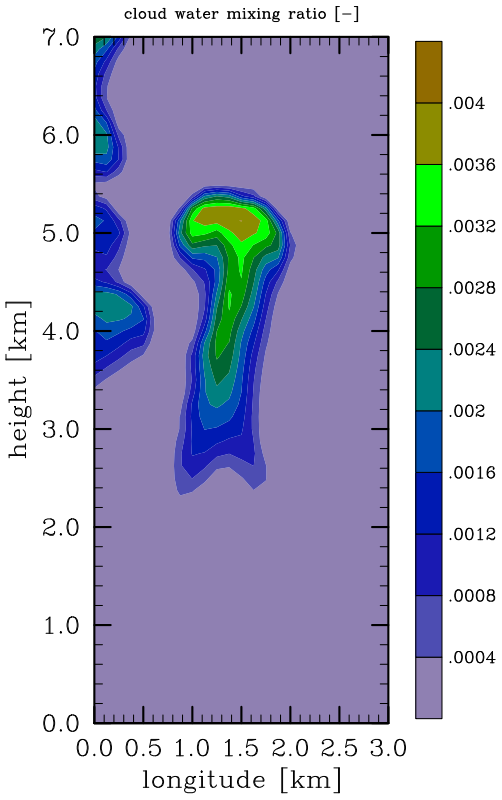

Figure 14: Cloud water mixing ratio of the vertical slice through w_{max}.

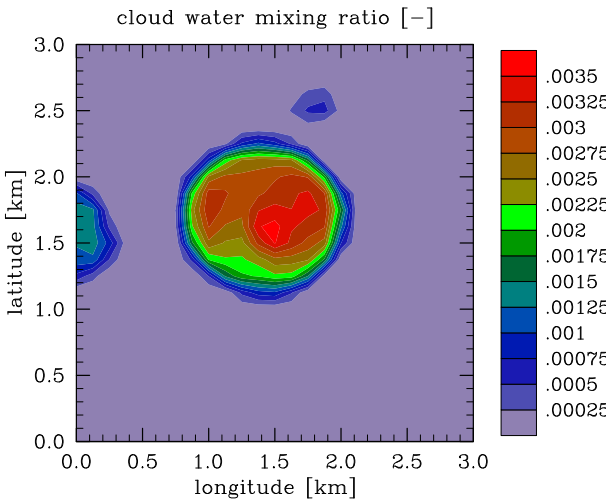

Figure 15: Cloud water mixing ratio of the horizontal slice through w_{max}.

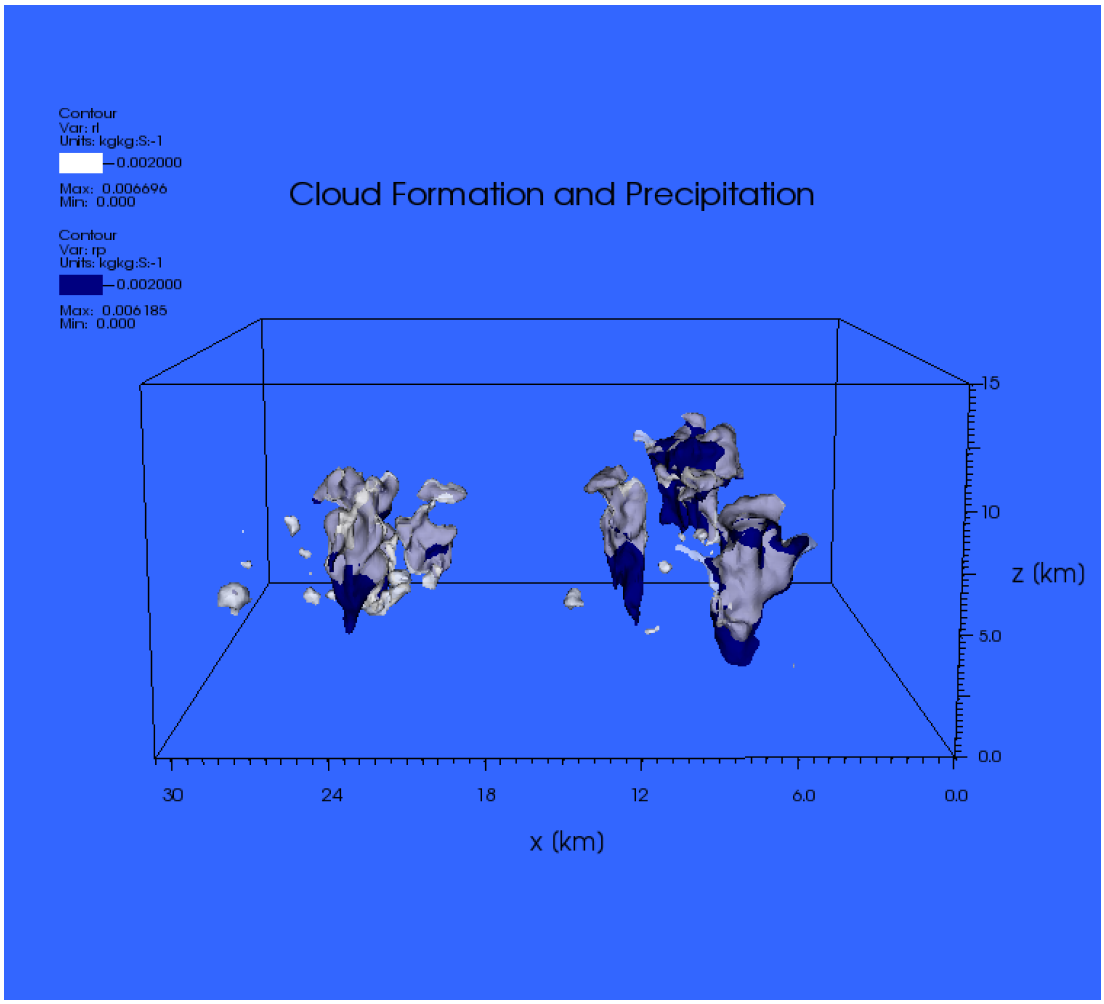

Figure 16: Cloud water and rain water mixing ratios for values greater than or equal to $2\,\mathrm{gkg}^{-1}$.

table's sample.

Figures 17 and 18 again show contour plots of w on vertical and horizontal slices through the maximum vertical velocity, respectively. This time we display the cross sections for the cloud around the global maximum of vertical velocity occuring throughout the whole computation. When examining the reference run with an output frequency of 10 min this global maximum of w amounting to $31\,\mathrm{ms}^{-1}$ is registered after four hours and fifty minutes of simulated time at a height of about 6 km (cp. table 1).
It can be seen that not all the towers are as compact as the one chosen for detailed analysis (cp. figures 6 and 8). On the other hand a compact column is not an exception either.

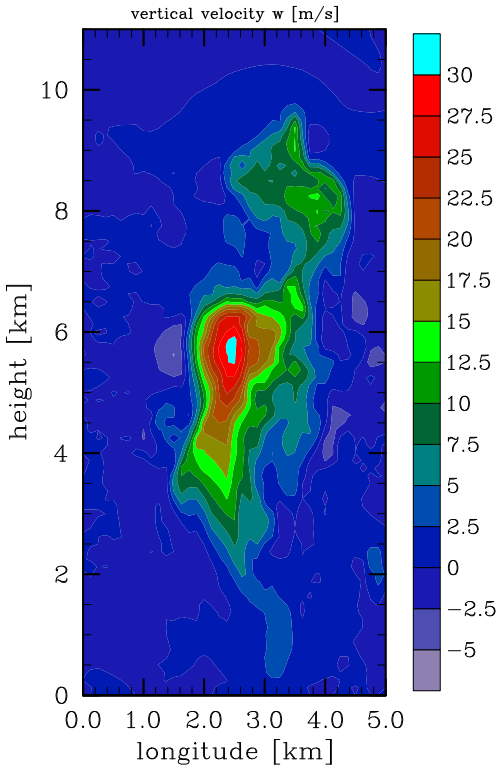

Figure 17: Vertical velocity of a vertical slice through the tower around w_{max} of the whole computation.

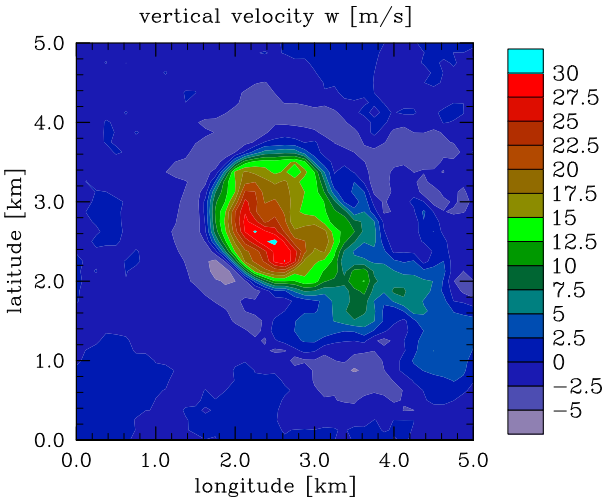

Figure 18: Vertical velocity of a horizontal slice through the tower around w_{max} of the whole computation.

t [h : min]	w_{max} [ms^{-1}]	u_{max} [ms^{-1}]	v_{max} [ms^{-1}]	$h_{w_{max}}$ [km]	Δz_{cloud} [km]	Δx_{cloud} [km]	Δy_{cloud} [km]
3 : 00	15.376	4.341	4.076	3.875	4.625	1.000	1.125
3 : 10	19.243	7.646	7.097	4.125	4.750	1.000	1.250
3 : 20	21.742	12.105	11.657	6.125	7.750	2.375	2.000
3 : 30	18.778	10.786	15.263	4.125	5.125	1.125	1.000
3 : 40	20.493	9.654	9.973	4.250	3.875	1.125	1.125
3 : 50	20.999	10.186	9.839	4.875	4.250	1.125	1.125
4 : 00	20.750	9.975	9.629	8.000	8.375	1.625	2.375
4 : 10	22.456	12.138	11.267	5.875	4.375	1.375	1.375
4 : 20	18.842	10.827	12.493	5.750	5.500	5.125	2.250
4 : 30	25.624	11.105	13.090	8.125	5.500	2.500	1.750
4 : 40	22.735	10.492	8.070	6.250	7.000	1.875	1.250
4 : 50	30.993	13.856	12.591	5.875	10.375	2.375	2.125
5 : 00	20.323	9.976	10.595	7.875	5.000	4.125	1.625
5 : 10	21.232	10.557	15.415	7.750	4.625	2.875	3.500
5 : 20	18.890	11.727	11.383	4.125	3.500	1.125	1.500
5 : 30	26.219	13.915	11.946	8.750	8.250	3.375	2.625
5 : 40	23.254	12.119	15.560	6.250	5.125	3.125	1.875
5 : 50	20.380	11.027	12.570	9.500	7.125	2.125	3.125
6 : 00	18.796	10.132	8.531	5.750	5.750	2.625	1.375
Ø	21.428	10.661	11.108	6.171	5.836	2.211	1.809

Table 1: Characteristic velocities and dimensions for the simulation with a spatial step size of 125 m.

We round this section off with contour plots of w on vertical and horizontal slices through w_{max} of two other columns chosen arbitrarily. Figures 19 and 20 show the plots for the tower around the local maximum vertical velocity after four hours of simulated time, figures 21 and 22 show the plots for the tower

around the local maximum vertical velocity after six hours of simulated time.

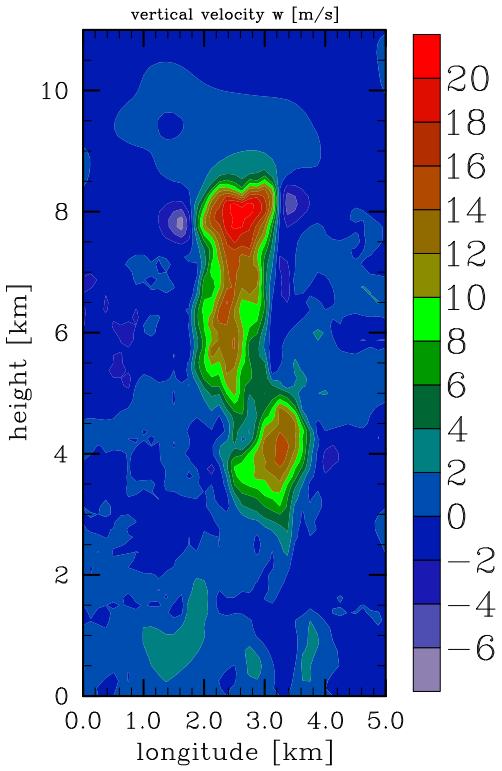

Figure 19: Vertical slice. $t = 4\,\mathrm{h}$, $w_{max} = 20.750\,\mathrm{ms}^{-1}$, $h_{w_{max}} = 8.000\,\mathrm{km}$.

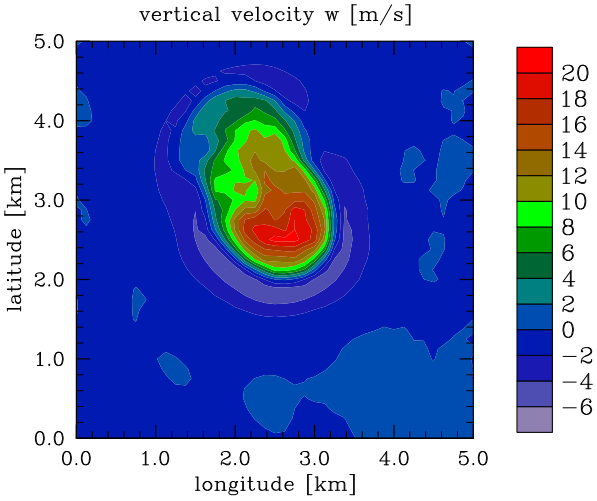

Figure 20: Horizontal slice. $t = 4\,\mathrm{h}$, $w_{max} = 20.750\,\mathrm{ms}^{-1}$, $h_{w_{max}} = 8.000\,\mathrm{km}$.

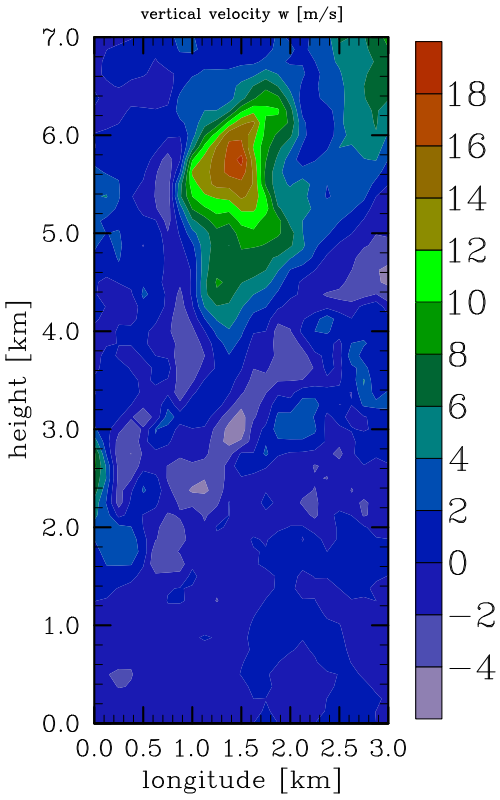

Figure 21: Vertical slice. $t = 6\,\mathrm{h}$, $w_{max} = 18.796\,\mathrm{ms}^{-1}$, $h_{w_{max}} = 5.750\,\mathrm{km}$.

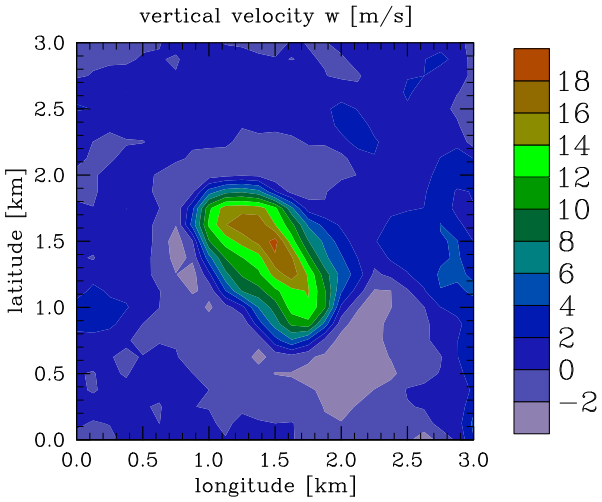

Figure 22: Horizontal slice. $t = 6\,\mathrm{h}$, $w_{max} = 18.796\,\mathrm{ms}^{-1}$, $h_{w_{max}} = 5.750\,\mathrm{km}$.

4 How to compare equations to data?

The basic idea for the comparison of the simulation data with the physical statements of the model equations is to extract the model's dependent variables from the code-output. These asymptotic unknowns can be quantities of leading order, as in the case of the vertical velocity $w^{(0)}$, or higher order perturbation quantities.

4.1 Extraction of the asymptotic quantities from the code-output

The asymptotic deep convective column model consists of two distinct systems of equations for the saturated and the undersatureted air regimes, respectively. In this report we concentrate on the evaluation of the saturated case while the undersaturated case is left for future investigations based on simulations including vertical wind shear. As the saturated setting is characterised by strong updrafts driven by the release of latent heat due to condensation, the vertical velocity data are used to filter the code-output. For a specific time-level, the maximum vertical velocity is detected. Starting from there, the vertical velocity values are checked moving horizontally outward up to the identification of the first value less or equal to zero. The inner area defines the horizontal extent of the cloud. In the vertical direction the cloud-subdomain contains all the grid points of the computational domain.

Concerning a particular physical quantity, the code-output at one specific grid point of the subdomain represents the total value of this quantity at that location. Hence in theory an asymptotic unknown can be calculated by subtracting the contributions of the lower orders of the asymptotic expansion from the respective simulation data.

Regarding the thermodynamic variable pressure, the asymptotic expansion reads as follows (p has to be expanded up to $p^{(6)}$ whereas $p^{(5)}$ does not appear in the final system of equations, see [1]):

$$p = p^{(0)} + \varepsilon p^{(1)} + \varepsilon^2 p^{(2)} + \varepsilon^3 p^{(3)} + \varepsilon^4 p^{(4)} + \varepsilon^6 p^{(6)}. \tag{19}$$

Consequently the perturbation part $p^{(6)}$ which is the dependent pressure variable in the asymptotic deep convective column model can be expressed as:

$$p^{(6)} = (p - p^{(0)} - \varepsilon p^{(1)} - \varepsilon^2 p^{(2)} - \varepsilon^3 p^{(3)} - \varepsilon^4 p^{(4)})\varepsilon^{-6}. \tag{20}$$

As $p^{(0)}$ up to $p^{(4)}$ are known analytically, $p^{(6)}$ could be computed by subtracting the ε-weighted analytical results from the code-output. For the purpose of the asymptotic model's plausibility check, however, we follow the guideline not to mix up code-output with external analytical results.

Thus the lower order contributions to total pressure inherent to the simulation data have to be figured out. The pressure parts $p^{(0)}$ to $p^{(4)}$ represent the hydrostatic background stratification and vary only with height, $p^{(6)}$ has to adjust in such a way that the divergence constraint from the continuity equation is fulfilled and therefore also varies horizontally.

Using code-output, the background stratification can be expressed by the pressure averaged horizontally over the whole computational domain. Subtracting this only z-dependent quantity from total pressure results in the pressure part also varying in the horizontal directions which corresponds to $p^{(6)}$. The evaluation of the simulation data is generally done after nondimensionalisation of the code raw data with the reference values used in the asymptotic analysis (see [1]). The scaling is not done with a fixed ε but by making use of the corresponding maximum Mach number of the cloud-subdomain. Hence $p^{(6)}$ is computed in the following way:

$$p^{(6)} = \left(p_{\text{code, subdomain}} - \overline{p}^{\text{hor}}_{\text{code}}\right) \frac{1}{M_{hor}^2}. \tag{21}$$

Analogously, the potential temperature $\theta^{(4)}$ is extracted from the code-output:

$$\theta^{(4)} = \left(\theta_{\text{code, subdomain}} - \overline{\theta}^{\text{hor}}_{\text{code}}\right) \frac{1}{M_{ver}^2}. \tag{22}$$

As we assume $\boldsymbol{v}_{\shortparallel}^{(0)} = 0$ (see [1]), the horizontal velocities $\boldsymbol{v}_{\shortparallel}^{(1)}$ are accessed via:

$$\boldsymbol{v}_{\shortparallel}^{(1)} = \boldsymbol{v}_{\shortparallel\,\text{code, subdomain}} \frac{1}{M_{hor}^{(1/3)}}. \tag{23}$$

To complete the set of asymptotic unknowns of the saturated air regime, the vertical velocity $w^{(0)}$ is still needed:

$$w^{(0)} = w_{\text{code, subdomain}}. \tag{24}$$

In order to evaluate all the terms appearing in the asymptotic model's balances, the basic state density $\varrho^{(0)}$ is missing as yet. As the explicit formula is to be avoided, $\varrho^{(0)}$ is expressed by the ideal gas law with the definition of potential temperature inserted. The hydrostatic values for potential temperature and pressure are again represented by their horizontally averaged simulation results:

$$\varrho^{(0)} = \frac{1}{\overline{\theta}^{\text{hor}}_{\text{code}}} \, \overline{p}^{\text{hor}}_{\text{code}}{}^{(1/\gamma)}. \tag{25}$$

In the model equations, the mixing ratios of the moisture species generally appear at leading order. The values computed by the code have to be referred to the appropriate reference values to obtain the asymptotic quantities.

4.2 Hydrostatics through analysis, asymptotics and numerics

As a preliminary step, the code's representation of hydrostatics is examined in order to provide a reliable basis for the described postprocessing strategy. In three differently stratified atmospheres, the hydrostatic pressure distribution is computed:

(a) For the hydrostatic state in a dry adiabatic atmosphere, we compare the analytic solution of the hydrostatics equation, its asymptotic solution and the solution by the code.

(b) For the hydrostatic state in a moist adiabatic atmosphere, the solution of the hydrostatics equation by numerical integration with MATLAB using an explicit fourth-order Runge-Kutta method, the asymptotic solution and the solution by the code are compared.

(c) For the hydrostatic state in an atmosphere stratified according to the sounding used for the simulations of this work, we compare the solution of the hydrostatics equation by numerical integration with MATLAB and the solution by the code.

(a)
As θ is constant, the hydrostatics equation

$$\frac{dp}{dz} = -\varrho \tag{26}$$

and the ideal gas law with the definition of potential temperature inserted

$$\varrho = \frac{1}{\theta}\, p^{(1/\gamma)} \tag{27}$$

result in an ordinary differential equation with p as the only unknown:

$$\frac{dp}{dz} = -\frac{1}{\theta}\, p^{(1/\gamma)}. \tag{28}$$

This ODE can be solved analytically and yields the following explicit formula for the pressure:

$$p(z) = \left(1 - \frac{\gamma - 1}{\gamma}\alpha z\right)^{\left(\frac{\gamma}{\gamma-1}\right)}. \tag{29}$$

The dimensionless parameter α in equation (29) originates from the nondimensionalisation process and reads as follows:

$$\alpha = \frac{l_{\mathrm{ref}} g}{\theta_{\mathrm{ref}} R_d} \approx 1.25\,. \tag{30}$$

This parameter also occurs in the asymptotic solution of equation (28). The leading order pressure for the dry adiabatic case is given by

$$p^{(0)}(z) = \exp(-\alpha z). \tag{31}$$

Based on the constant potential temperature field, the code computes its hydrostatic pressure distribution.

Figure 23 shows the analytic, the asymptotic and the code's solution of the hydrostatics equation in a dry adiabatically stratified atmosphere.

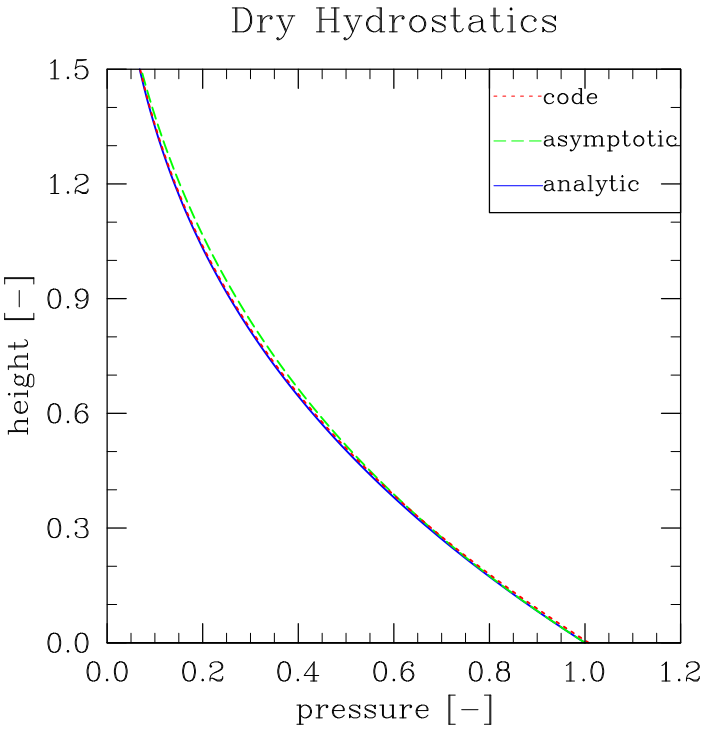

Figure 23: Pressure distribution in a dry adiabatic atmosphere as it results from solving the hydrostatics equation analytically, asympotically and by the code.

(b)
In addition to equations (26) and (27) the condition for moist adiabaticity is needed, which is a consequence of the transport equation for potential temperature:

$$\frac{\partial \theta}{\partial z} = \frac{1-\gamma}{\gamma} \frac{\theta \varrho}{p} L \frac{\partial r_{vs}}{\partial z}. \tag{32}$$

Inserting the equation of state (27) into equation (32) leads to

$$\frac{\partial \theta}{\partial z} = \frac{1-\gamma}{\gamma} p^{\left(\frac{1-\gamma}{\gamma}\right)} L \frac{\partial r_{vs}}{\partial z}, \tag{33}$$

providing – together with equation (28) – a system of two ODEs with two unknowns, namely potential temperature θ and pressure p, that is solved numerically. In doing so, the saturation vapour mixing ratio r_{vs} is given by the formulation in terms of the saturation vapour pressure whose temperature dependence in turn is described by the Clausius-Clapeyron-equation (see [1]):

$$r_{vs} = \frac{R \exp\left[A\left(1 - \frac{1}{\theta}\left(\frac{1}{p}\right)^{\left(\frac{\gamma-1}{\gamma}\right)}\right)\right]}{p - P \exp\left[A\left(1 - \frac{1}{\theta}\left(\frac{1}{p}\right)^{\left(\frac{\gamma-1}{\gamma}\right)}\right)\right]}\,. \tag{34}$$

The asymptotic solution for the pressure field determined by the system of equations (28) and (33) is at leading order identical to that for the dry adiabatic stratification and hence given by equation (31). The moisture processes come into play from the second asymptotic order onwards.

In order to obtain the code's solution for the pressure field, the potential temperature distribution provided by numerical integration and the water vapour mixing ratios computed with θ and p - both resulting from numerical integration of equations (28) and (33) - are passed to the code as input data.

The numerical, the asymptotic and the code-based representations of the hydrostatic state in a moist adiabatically stratified atmosphere are plotted in figure 24.

Additionally it is checked whether the code preserves a given basic state that is already in hydrostatic balance. For this purpose the potential temperature and pressure fields obtained numerically are passed to the code as well as the resultant values for r_{vs}. Examination of the output after one time step shows that the pressure profile is identical to the input and with it also to the pressure distribution calculated by the code on its own starting from the moist adiabatic θ and r_{vs}. The velocities remain zero as well.

(c)
We insert the potential temperature profile used for the deep convective simulations into equation (28) and obtain in this way an ODE with pressure as the only unknown. This ODE is solved by numerical integration with an explicit fourth-order Runge-Kutta method.

The resulting pressure field is compared to that produced by the code on the basis of the same potential temperature profile and the values of the water vapour mixing ratio (see section 3.2).

In figure 25 the curves of the hydrostatic pressure in the backgroung stratifica-

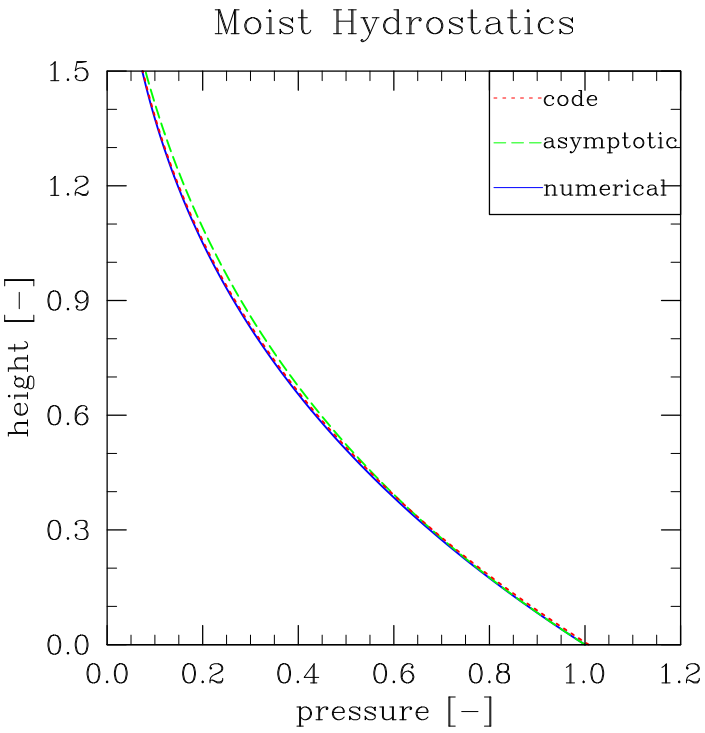

Figure 24: Pressure distribution in a moist adiabatic atmosphere as it results from solving the hydrostatics equation numerically, asympotically and by the code.

tion of the simulations can be found; they result from fourth-order numerical integration and from computation with the code respectively.

A comparison of the hydrostatic states in the dry adiabatic, the moist adiabatic and the sounding's stratifications respectively on the basis of the pressure fields provided by the code is shown in figure 26. It reflects the slight difference between the dry and the moist case already seen in the asymptotic analysis where the contributions of the moisture processes do not occur until the second order. The potentially unstable stratification of the sounding shows a smaller absolute value of the pressure gradient dp/dz than both adiabatic curves.

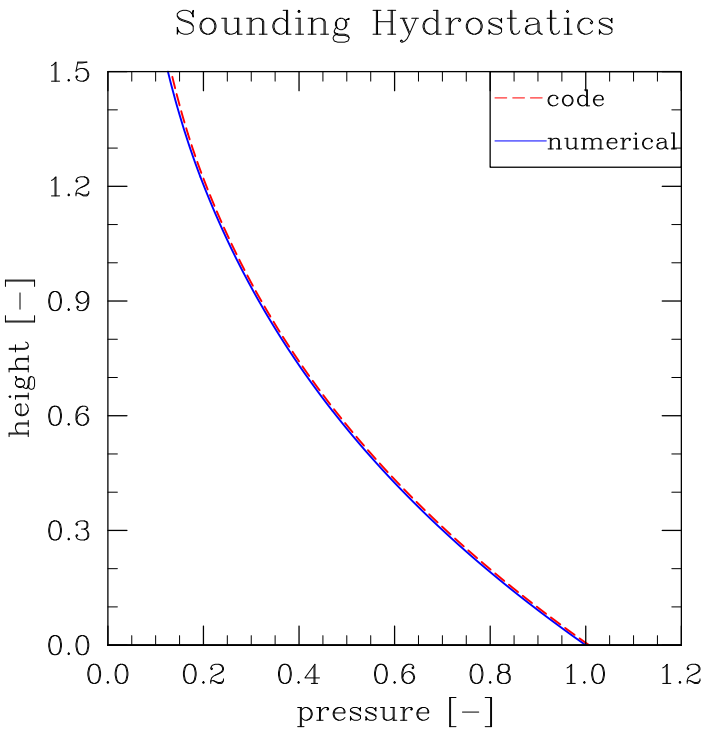

Figure 25: Pressure distribution in an atmosphere stratified according to the sounding used for the simulations as it results from solving the hydrostatics equation numerically and by the code.

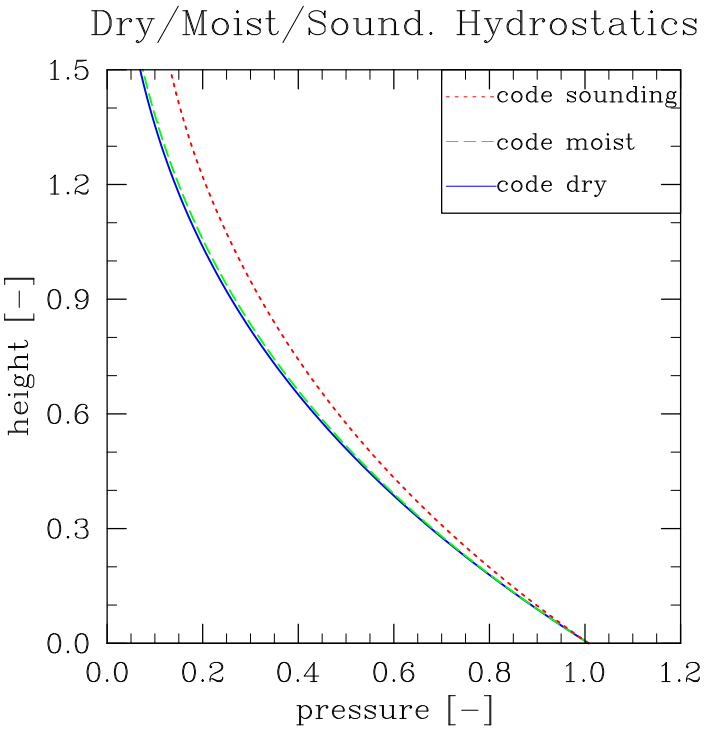

Figure 26: Hydrostatic pressure distribution for the dry adiabatic, the moist adiabatic and the sounding's stratification computed by the UCLA-LES-Code.

4.3 Compliance with the divergence constraint

During a run with the code, pressure is adjusted in such a way that the resulting velocity field satisfies the discretised version of the continuity equation to machine accuracy. This anelastic divergence constraint in its continous formulation reads:

$$\nabla \cdot (\varrho_0 \boldsymbol{v}) = 0. \tag{35}$$

As the basic state density ϱ_0 only varies with height, equation (35) can equivalently be written as:

$$\varrho_0 \nabla_{\shortparallel} \cdot \boldsymbol{v}_{\shortparallel} + (\varrho_0 w)_z = 0. \tag{36}$$

In order to check whether the compliance of the velocity field with the anelastic divergence constraint can be reproduced during postprocessing, we use the same discretisation for the continuity equation as in the code. Herein the differential quotients are discretised by a second order centered finite difference approximation.

The code uses a staggered grid where velocities are located on the cell faces while pressure and density reside in the cell centres. Thus formulating the product of density and vertical velocity requires the interpolation of ϱ_0 on the respective w-face. The product of density and the horizontal divergence of the horizontal velocity vector, however, can be built without any interpolation because ϱ_0 does not vary horizontally. The centered difference quotients of second order are constructed around the cell centres using the code raw data on the cell faces, i.e. the stencil's spacing is $2\,\frac{\Delta x}{2} = \Delta x$. As the grid is equidistant, the same spacing is valid in all three spatial directions.

The scatter plot in figure 27 shows the accumulated continuity equation, i.e. the terms appearing on the left hand side of equation (36) are discretised in the way described above and added up: For each height-level all the values of the corresponding cross section of the cloud-subdomain are plotted. As the horizontal extent of the cloud-subdomain consists of ten grid points in both directions, one hundred values belong to each height level.
It can be seen that the divergence constraint is fulfilled to an accuracy of $2\,\mathrm{x}\,10^{-8}$. In order to judge this order of magnitude, we have a look at the normalised divergence, i.e. the sum of the terms in equation (36) is referred to the sum of their absolute values. For the exact compliance with the divergence constraint this quotient equals zero since the numerator becomes zero. Otherwise it takes values between the minimum of -1.0 and the maximum of $+1.0$.

Figure 28 shows that by far the largest part of the points scores lies between -10^{-6} and $+10^{-6}$. The whole scatter covers the interval from $-9\,\mathrm{x}\,10^{-6}$ to

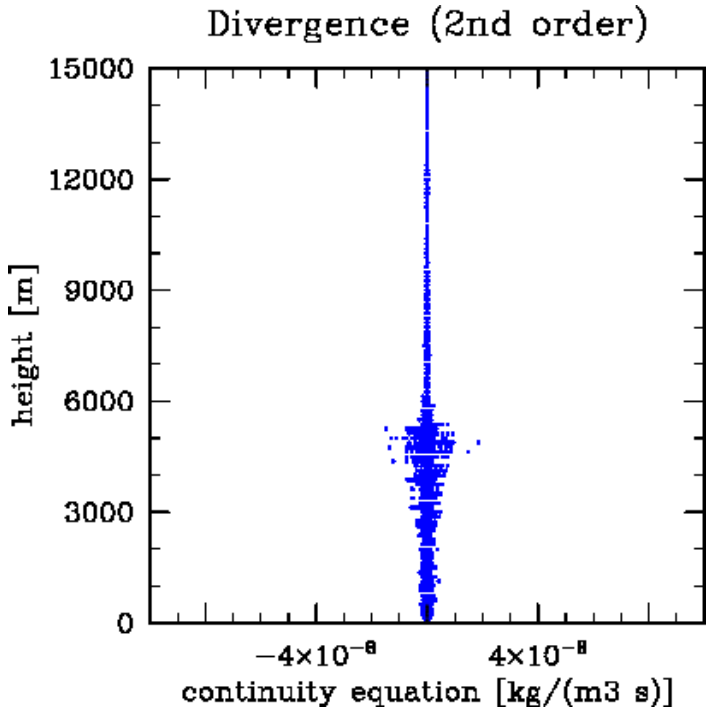

Figure 27: Accumulated continuity equation of the cloud-subdomain; second order discretisation with Δx-spacing of the stencil.

$+9\,\mathrm{x}\,10^{-6}$.

Using a discretisation that is also second order accurate but different from that used for the divergence in the UCLA-LES-Code leads to quite different results. At first velocities are interpolated to the cell centres, then the centered difference quotients are constructed around the cell centres using the code raw data of the neighbouring cell centres, i.e. the stencil's spacing is $2\,\Delta x$.

As figure 29 reveals, the divergence constraint in this case is merely fulfilled to an accuracy of $2\,\mathrm{x}\,10^{-2}$.

The scatter plot of the normalised divergence in figure 30 covers the entire interval from -1.0 to $+1.0$. Only in the upper part of the atmosphere, i.e. above the cloud top, the points scores are more concentrated around zero, namely in the interval between $-2\,\mathrm{x}\,10^{-1}$ and $+2\,\mathrm{x}\,10^{-1}$.

Using a fourth order centered finite difference scheme to discretise the divergence (spacing of the stencil: $4\,\Delta x$) produces nearly the same results as the second order scheme with the $2\,\Delta x$-spacing of the stencil.

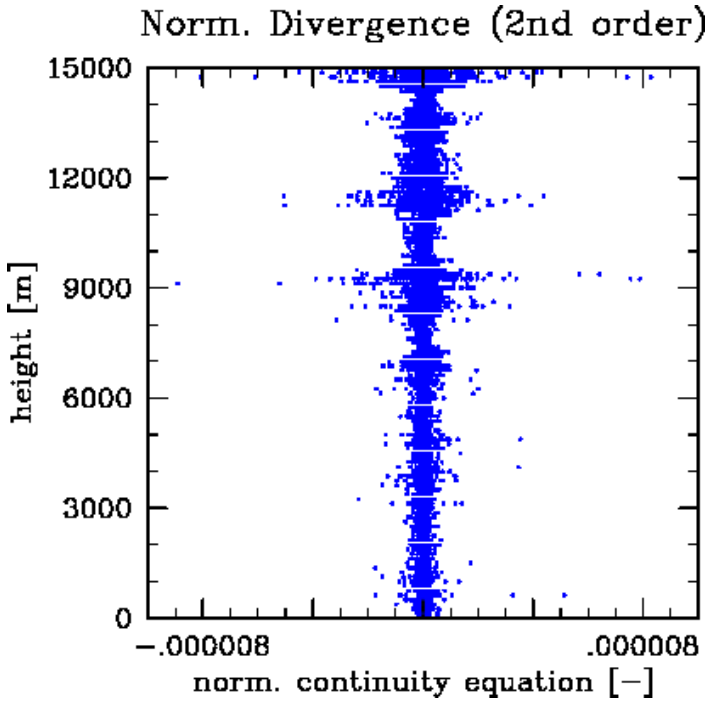

Figure 28: Accumulated and normalised continuity equation of the cloud-subdomain; second order discretisation with Δx-spacing of the stencil.

From these observations we conclude that it is essential for the reproduction of code-results during postprocessing to use the same discretisations as in the code. This issue emerges again during the analysis of the asymptotic momentum balance (cp. section 5).

Remark:
The investigation of the continuity equation in this section is accomplished by means of equation (36) in conjunction with the code raw data. In the continuity equation of the asymptotic model (see section 2), however, velocities appear in different asymptotic orders, gradients are built on different length scales. As described in section 4.1, the evaluation of the asymptotic model equations is generally done after nondimensionalisation of the code raw data with the appropriate reference values and scaling according to the respective powers of the expansion parameter.

In the case of the continuity equation, the scalings of the horizontal divergence operator and the horizontal velocity vector cancel each other. Hence we are left with a nondimensionalisation which corresponds to a multiplication of each term in the equation by a factor of 8×10^2. For the exact compliance with the divergence constraint this factor has no consequences. Concerning a discrete divergence constraint, however, that is fulfilled to some finite accuracy only, this

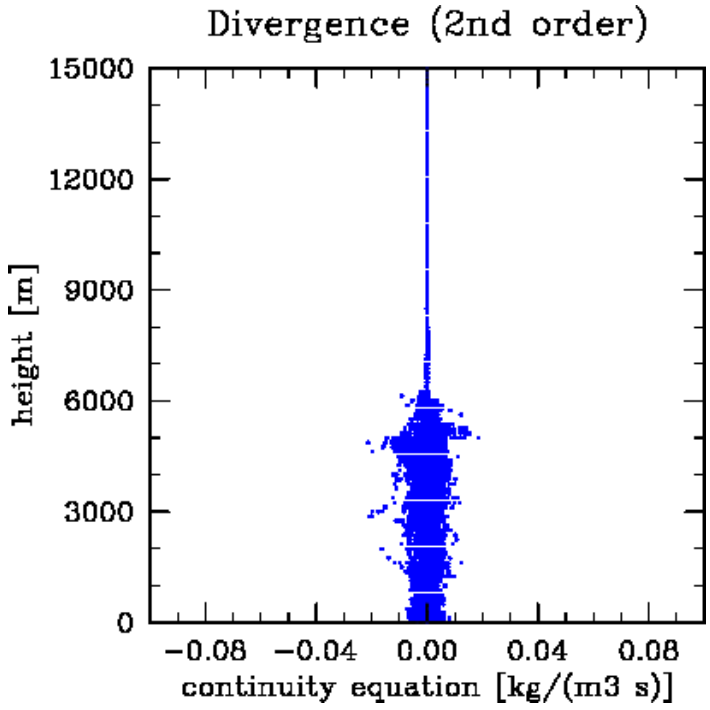

Figure 29: Accumulated continuity equation of the cloud-subdomain; second order discretisation with $2\,\Delta x$-spacing of the stencil.

factor is directly reflected in the result of the accumulated balance equation.

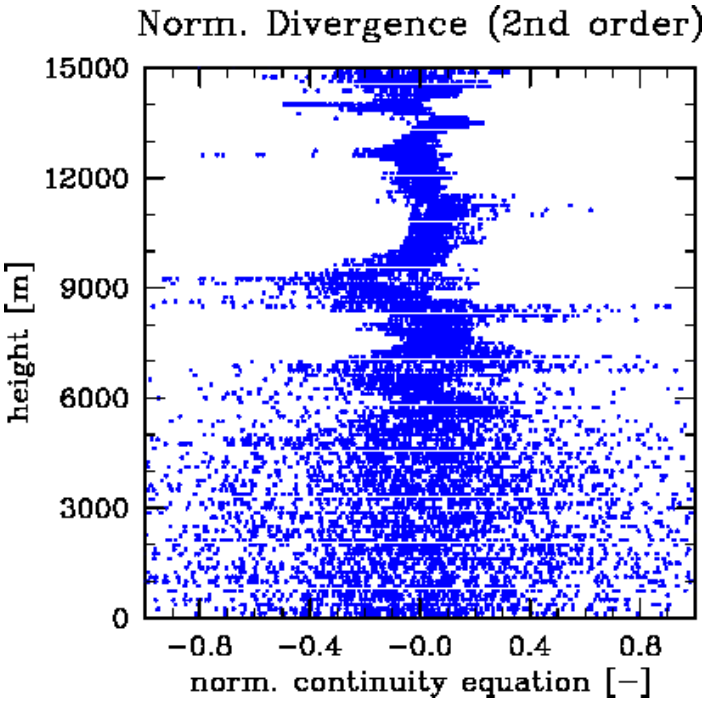

Figure 30: Accumulated and normalised continuity equation of the cloud-subdomain; second order discretisation with $2\,\Delta x$-spacing of the stencil.

5 Discussion of the results

The main data basis for the discussion in this section is provided by the subdomain of the deep convective column shown in figures 6 and 8.

As stated in section 4.1, the nondimensionalisation of the code raw data is done with the reference values used in the asymptotic analysis, the scaling of the dimensionless quantities is done with the corresponding maximum Mach number of the cloud-subdomain.

5.1 The asymptotic unknowns

In this section we show the distributions over height of the asymptotic perturbation quantities extracted from the simulation data. The graphs illustrate that the values of the asymptotic variables in the cloud region are of $\mathcal{O}(1)$.

Figure 31 shows the distribution of the leading order vertical velocity $w^{(0)}$. In order to obtain the corresponding dimensional quantity, we would have to multiply by the reference value of $10\,\mathrm{ms}^{-1}$.

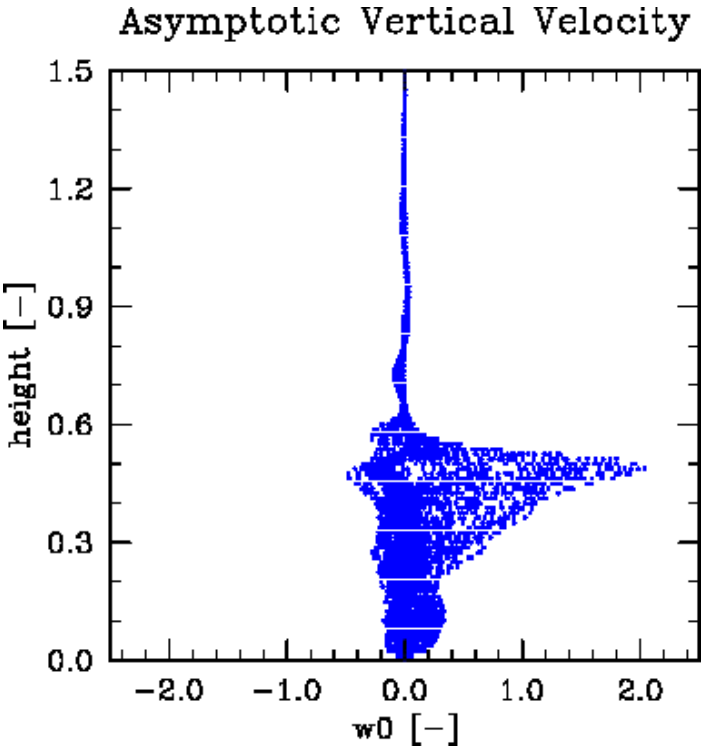

Figure 31: Leading order vertical velocity $w^{(0)}$ of the cloud-subdomain.

The vertical velocity profile reflects very well the cloud's vertical extent and structure. From the cloud base at about 2000 m upwards, the vertical velocity

continously increases up to its maximum of 21 m/s in the upper cloud part at about 5000 m. From there vertical velocity decreases and reaches 0 m/s at the cloud top at 6500 m.

Figure 32 provides the scatter plot of $p^{(6)}$, the pressure part guaranteeing compliance with the divergence constraint from the continuity equation.

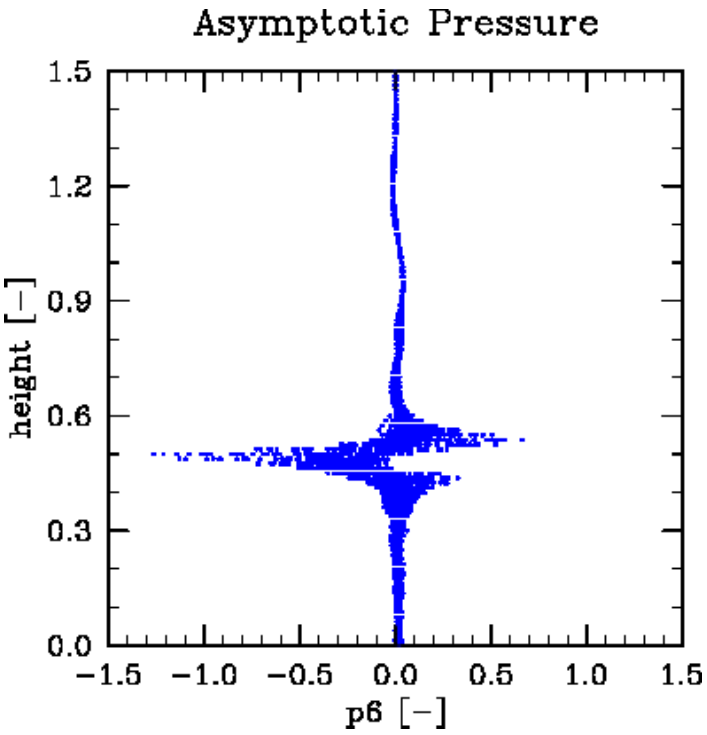

Figure 32: Asymptotic perturbation pressure $p^{(6)}$ of the cloud-subdomain.

This pressure profile is characterised by the sharp changes of sign of the vertical gradient before and after the maximum of vertical velocity discussed in figure 31.

In figure 33 the absolute value of the first order horizontal velocity vector $\boldsymbol{v}_{\shortparallel}^{(1)}$ is plotted. In order to obtain the corresponding dimensional quantity, we would have to multiply by the scaled reference value of $M_{hor}^{(1/3)} \cdot 10\,\mathrm{ms}^{-1} = 0.3 \cdot 10\,\mathrm{ms}^{-1} = 3\,\mathrm{ms}^{-1}$.
The maximum of the absolute value of horizontal velocities arises shortly above the maximum of vertical velocity where pressure attains its maximum (cp. figure 32), and the air is displaced outwards. Above the maximum there is a very steep negative gradient leading to a region with little horizontal motion at the cloud top.

Below the maximum of vertical velocity the absolute value of horizontal velocities is also relatively large. This is physically consistent because at that level a considerable air flow has to move towards the cloud centre in order to

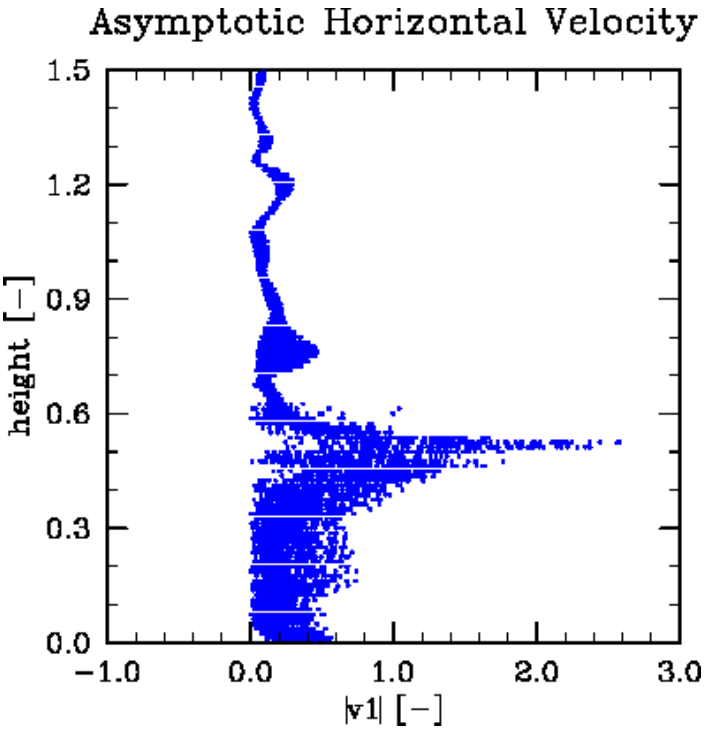

Figure 33: Absolute value of the asymptotic horizontal velocity vector $\boldsymbol{v}_{\shortparallel}^{(1)}$ of the cloud-subdomain.

compensate the mass transport upwards which is reflected in the minimum of pressure.

These observations underline clearly that pressure controls the horizontal flow, one of the conclusions of the reduced asymptotic model.

Figure 34 represents the asymptotic model's potential temperature $\theta^{(4)}$.

It can be seen that potential temperature continously increases because of the latent heat release due to condensation. Once all the water vapour has been condensed there is no more heating and hence no vertical acceleration. This level corresponds to the height of the vertical velocity maximum.

The distribution of leading order vertical velocity $w^{(0)}$ in figure 31 perfectly correlates with the potential temperature deviation from the background stratification represented by $\theta^{(4)}$. This approves another result of the asymptotic analysis: In the saturated column vertical velocity is directly determined by the buoyancy induced by potential temperature differences between inside the column and outside.

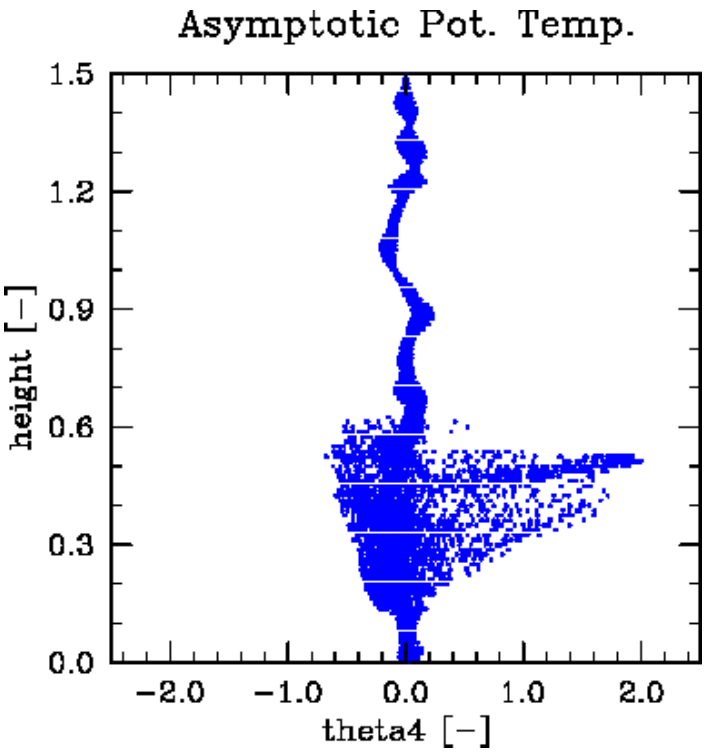

Figure 34: Asymptotic perturbation potential temperature $\theta^{(4)}$ of the cloud-subdomain.

Figure 35 shows the distribution over height of the leading order vertical velocity $w^{(0)}$ in conjunction with the perturbation pressure part $p^{(6)}$.
As discussed above, horizontal velocities directly follow the shape of the pressure profile.

Figure 35 illustrates impressively that the leading order vertical velocity, however, is developing freely independent of pressure over the whole depth of the convective column, one of the main statements of the reduced asymptotic model; only the horizontal divergence is controlled by a pressure field.

Pressure fluctuations of order $\frac{\varrho w^2}{p}$ would be the fluctuations normally expected if vertical velocity inertia was comparable to the pressure fluctuation gradients. That would mean variations of $p^{(4)} = \mathcal{O}(1)$, i.e. pressure variations by ε^{-2} larger than those actually observed.

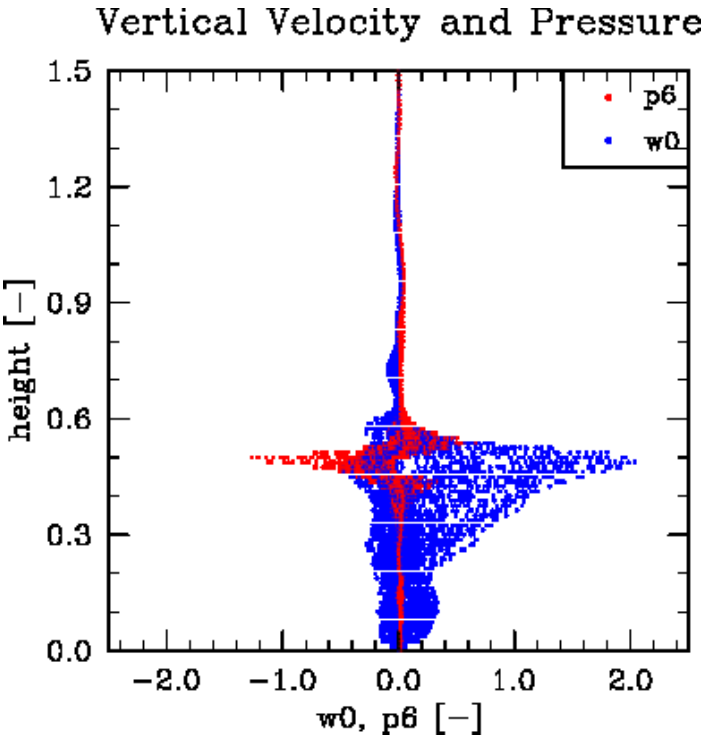

Figure 35: Leading order vertical velocity $w^{(0)}$ and asymptotic perturbation pressure $p^{(6)}$ of the cloud-subdomain.

5.2 The asymptotic vertical momentum balance

The asymptotic column model analysed in this report represents a closed system of equations for the leading order vertical velocity in deep convective clouds. In this section we have a detailed look at the terms in the asymptotic vertical momentum balance.

Figure 36 shows the individual terms of the vertical momentum balance.

In order to demonstrate the structure of each term, the plots do not have the same scales. Spatial gradients are approximated using a second order discretisation with a Δx-spacing of the stencil (cp. section 4.3).

The first four scatter plots display the time derivative, vertical and horizontal advection and buoyancy, i.e. the terms contained in the asymptotic vertical momentum balance.

The asymptotic model does not include the physical process of turbulent friction.[3] The turbulence term representing the sub-filter scale contribution to momentum, however, is an inherent part of the momentum equations solved by the code. As we reconstruct the vertical momentum balance with quantities extracted from the code output, we have to complete the balance by the respective turbulence term. The distribution over height of this term is shown in the fifth plot of figure 36.

In order to judge the possible influence of the pressure deviation from the background on the evolution of vertical velocity, the sixth plot of figure 36 yields the vertical gradient of $p^{(6)}$ where the scaling is done by the vertical Mach number.

It can be seen that the time derivative and advection terms are of the same order of magnitude that is by a factor of ten larger than the order of magnitude of the buoyancy, turbulence and pressure gradient terms.

In figure 37 the terms of the asymptotic vertical momentum balance – i.e. the individual plots of figure 36 – are added up successively.

In order to judge the contribution of each term to the whole balance, all the plots have got the same scales. We observe that the sum of the terms is smaller than the time derivative and advection terms themselves. As the discrete balance is not fulfilled exactly but only to some finite accuracy, nondimensionalisation is directly reflected in the result of the accumulated balance equation (see remark

[3] This process could be considered by including a turbulence parameterization in the set of equations for the asymptotic analysis, i.e. in the same way as microphysics is accounted for.

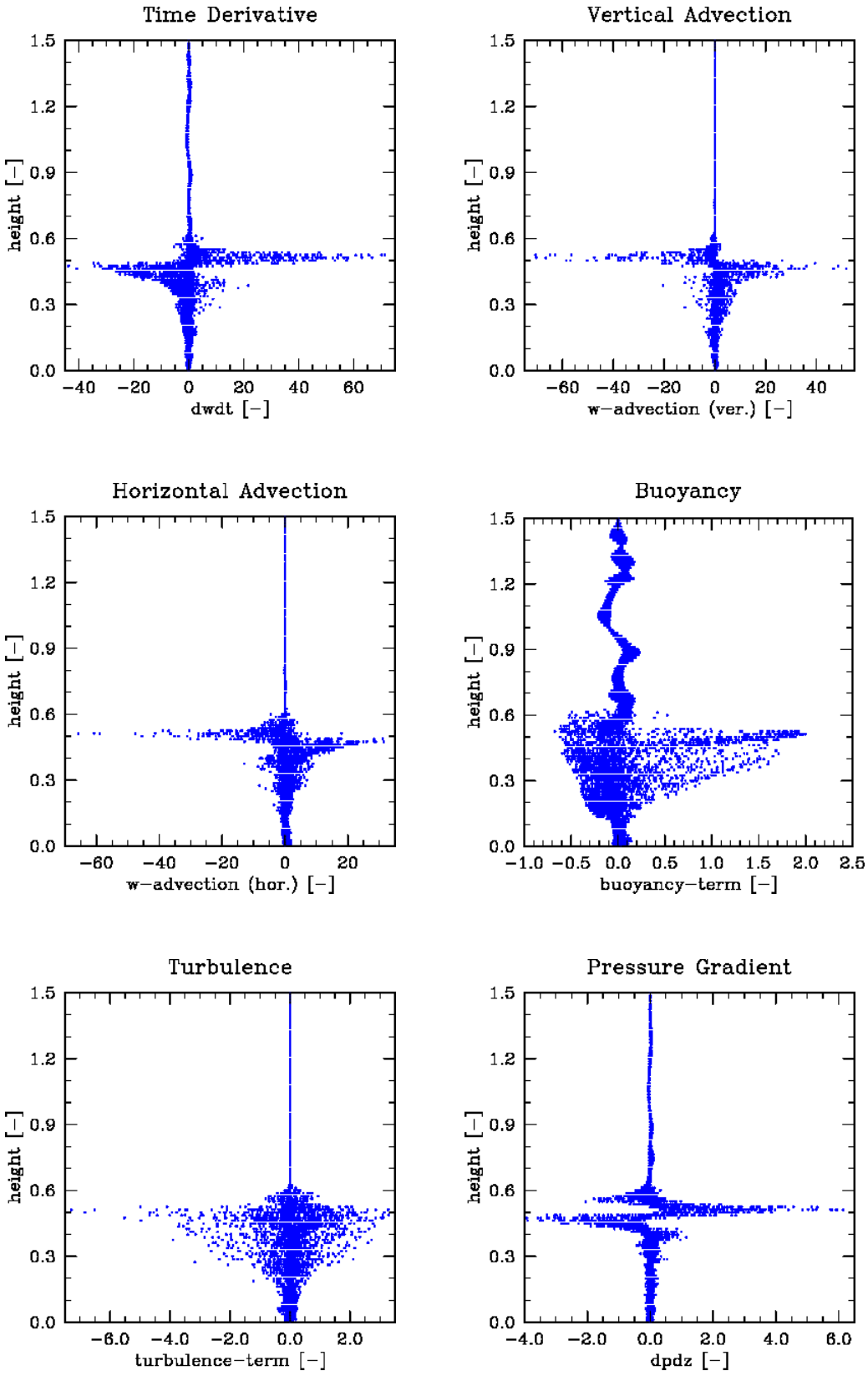

Figure 36: Individual terms of the vertical momentum balance. First row: Time Derivative: $w_t^{(0)}$, Vertical Advection: $w^{(0)}w_z^{(0)}$. Second row: Horizontal Advection: $\boldsymbol{v}_{\shortparallel}^{(1)} \cdot \nabla_{\boldsymbol{\xi}} w^{(0)}$, Buoyancy: $\theta^{(4)} - \theta_{\text{out}}^{(4)}$. Third row: Turbulence: $\frac{1}{\varrho_0}\nabla \cdot (\varrho_0 \vec{\vec{\tau}})$, Pressure Gradient: $p_z^{(6)}$.

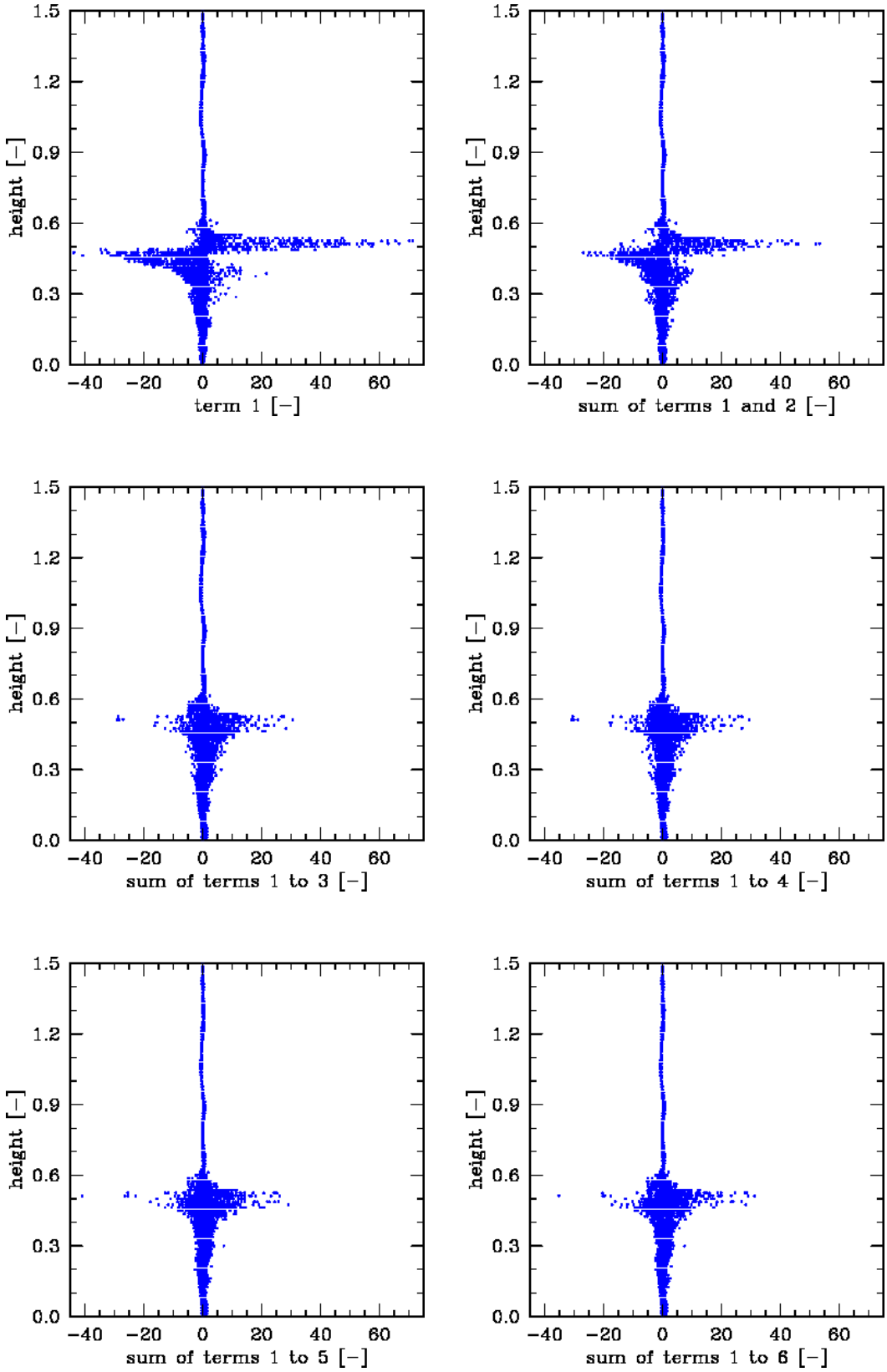

Figure 37: Vertical momentum balance, added up successively. First row: $w_t^{(0)}$ and $w_t^{(0)} + w^{(0)} w_z^{(0)}$. Second row: $w_t^{(0)} + w^{(0)} w_z^{(0)} + \boldsymbol{v}_{\shortparallel}^{(1)} \cdot \nabla_{\boldsymbol{\xi}} w^{(0)}$ and $w_t^{(0)} + w^{(0)} w_z^{(0)} + \boldsymbol{v}_{\shortparallel}^{(1)} \cdot \nabla_{\boldsymbol{\xi}} w^{(0)} - (\theta^{(4)} - \theta_{\text{out}}^{(4)})$. Third row: $w_t^{(0)} + w^{(0)} w_z^{(0)} + \boldsymbol{v}_{\shortparallel}^{(1)} \cdot \nabla_{\boldsymbol{\xi}} w^{(0)} - (\theta^{(4)} - \theta_{\text{out}}^{(4)}) - \frac{1}{\varrho_0} \nabla \cdot (\varrho_0 \vec{\boldsymbol{\tau}})$ and $w_t^{(0)} + w^{(0)} w_z^{(0)} + \boldsymbol{v}_{\shortparallel}^{(1)} \cdot \nabla_{\boldsymbol{\xi}} w^{(0)} - (\theta^{(4)} - \theta_{\text{out}}^{(4)}) - \frac{1}{\varrho_0} \nabla \cdot (\varrho_0 \vec{\boldsymbol{\tau}}) + p_z^{(6)}$.

at the end of section 4.3). In this case looking at the dimensional form of the equation would result in a sum that is by a factor of 10^{-2} smaller.

Figures 38 to 40 compare the accumulated vertical momentum balance for three different discretisations of the advection terms: Two second order discretisations (one with a Δx- and one with a $2\,\Delta x$-spacing of the stencil) and one fourth order discretisation with a $4\,\Delta x$-spacing of the stencil.
We observe that all three discretisations produce nearly the same results, the shape of the scatter becomes somewhat more compact with growing spacing of the stencil and higher accuracy. As the code does not use the same discretisation for divergence constraint and momentum advection, it cannot be expected that the second order finite difference scheme with the Δx-spacing of the stencil that leads to high accuracy concerning the compliance with the divergence constraint during postprocessing also produces comparable results with regard to momentum advection.

Figure 41 shows time derivative and vertical advection of the vertical momentum balance as individual terms along the centreline of the cloud, i.e. along the vertical line through the maximum of vertical velocity.

In figure 42 the sum of these two terms is displayed.

On the centreline of the cloud time derivative and vertical advection of vertical velocity nearly balance each other. This means that the dynamics on the centreline can approximatively be described by the inviscid Burgers' equation:

$$w_t^{(0)} + w^{(0)} w_z^{(0)} = 0. \tag{37}$$

Although we observe simple wave propagation the potential for shock formation is hence given [8] (and indeed, steep gradients of w near the cloud top do arrise).

To round this section off, we present the analysis of a cloud different to that used for discussion so far. By means of the accumulated vertical momentum balance we show that the result does not differ considerably when we examine another deep convective column than that of figures 6 and 8. Exemplarily we analyse the column of figures 17 and 18. This is the column around the global maximum of vertical velocity of the whole computation, the global w_{max} column.

In analogy with figure 38 the spatial gradients for the scatter plot of the global w_{max} column are approximated using the second order discretisation with the Δx-spacing of the stencil. Figure 43 reflects the shape of the global w_{max} column. The range of the main part of the points scores is of the same order of magnitude as for the column analysed before.

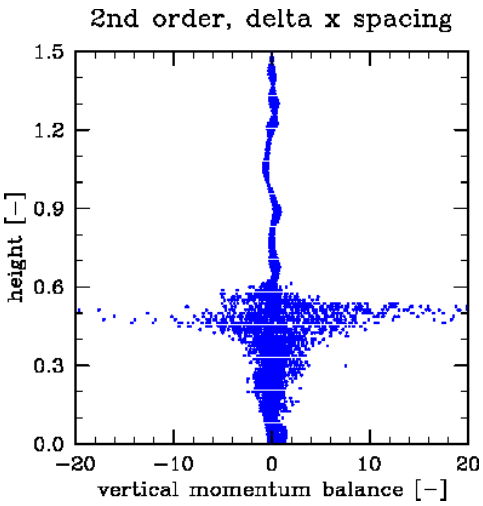

Figure 38: Accumulated vertical momentum balance of the cloud-subdomain; second order discretisation with Δx-spacing of the stencil.

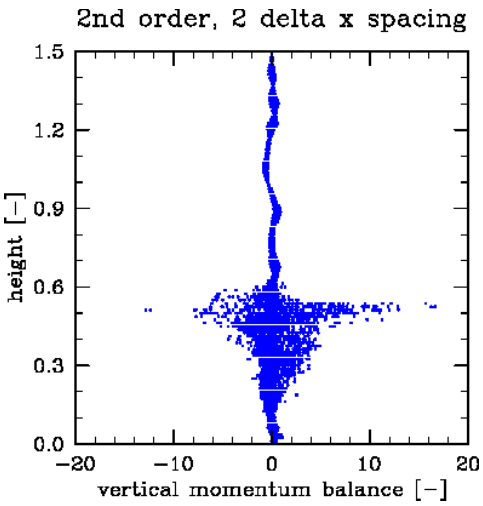

Figure 39: Accumulated vertical momentum balance of the cloud-subdomain; second order discretisation with $2\,\Delta x$-spacing of the stencil.

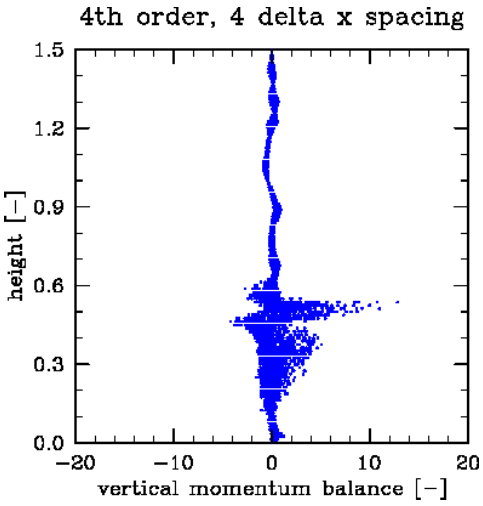

Figure 40: Accumulated vertical momentum balance of the cloud-subdomain; fourth order discretisation with $4\,\Delta x$-spacing of the stencil.

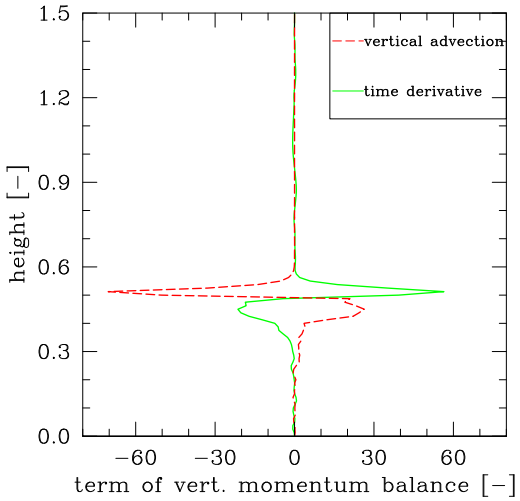

Figure 41: Time derivative ($w_t^{(0)}$) and vertical advection ($w^{(0)}w_z^{(0)}$) of the vertical momentum balance on the centreline of the cloud.

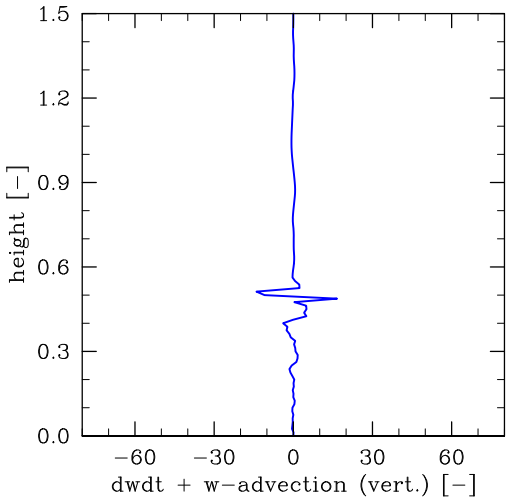

Figure 42: Sum of time derivative and vertical advection ($w_t^{(0)} + w^{(0)}w_z^{(0)}$) of the vertical momentum balance on the centreline of the cloud.

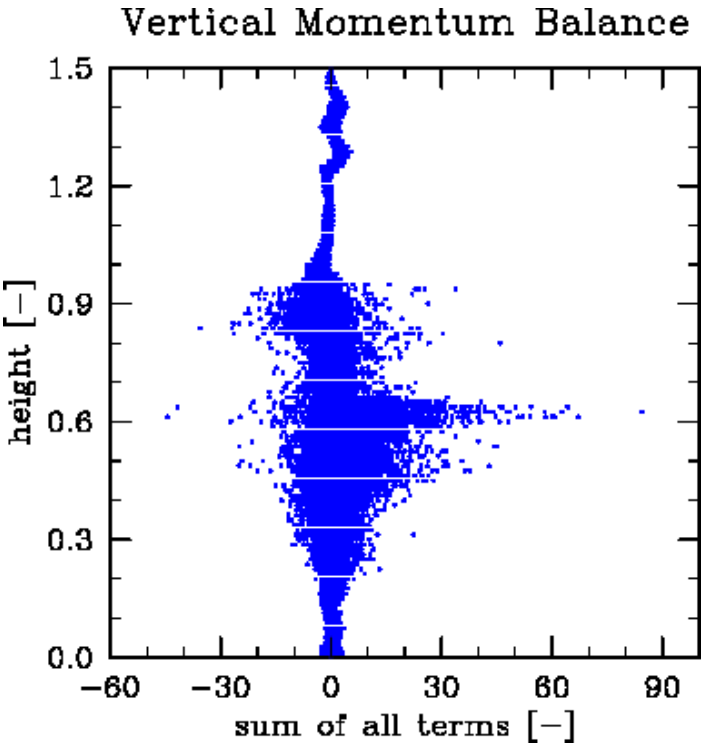

Figure 43: Accumulated vertical momentum balance for the global w_{max} column of the reference run.

5.3 Simulation with higher spatial resolution

For the discussion in this section we perform a computation with half the grid size, i.e. the equidistant step size amounts to 62.5 m in all directions. Besides this, the setting is the same as described in section 3.2.

It has to be emphasised that changes in the spatial resolution of the computational grid influence the stochastic behaviour of cloud formation. Therefore no direct comparison between low and high resolution is possible because the same columns as in the usual setting do not occur any more.

We investigate the deep convective column forming around the global maximum of vertical velocity, the global w_{max} column. In the computation with higher spatial resolution the global maximum of vertical velocity amounts to 29.395 ms^{-1} and is observed after five hours and forty minutes of simulated time (output frequency: 10 min) at a height of 7.063 km.

At first we follow the question whether a higher resolution has an impact on the result of the accumulated balance. Figure 44 provides the scatter plot of the accumulated vertical momentum balance for the highly resolved simulation.

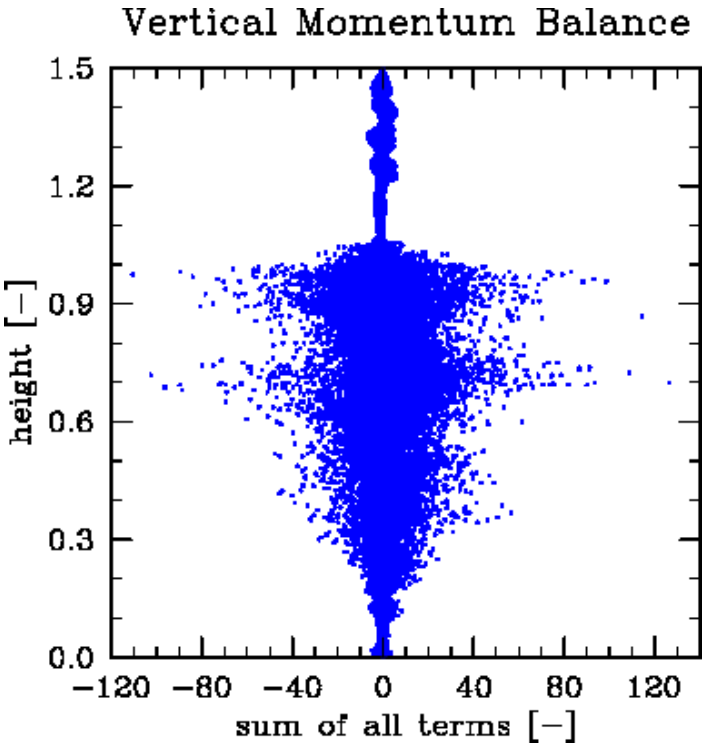

Figure 44: Accumulated vertical momentum balance for the global w_{max} column of the simulation with a spatial step size of 62.5 m.

The corresponding scatter plot for the global w_{max} column of the simulation with a spatial step size of 125 m is figure 43. Both plots do not show considerable differences regarding the order of magnitude of the accumulated balance. We conclude that the higher spatial resolution during the computation does not lead to a more accurate approximation of the spatial gradients during postprocessing.

Figures 45 and 46 show the usual contour plots of w on vertical and horizontal slices through the cloud region, respectively. (For comparison: The contour plots of the global w_{max} column for the simulation with low resolution are figures 17 and 18).

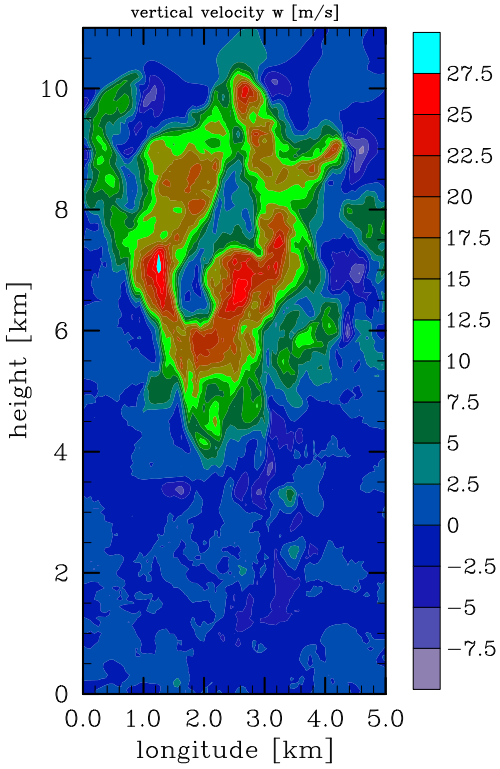

Figure 45: Vertical slice of the global w_{max} column from the computation with a spatial step size of 62.5 m.

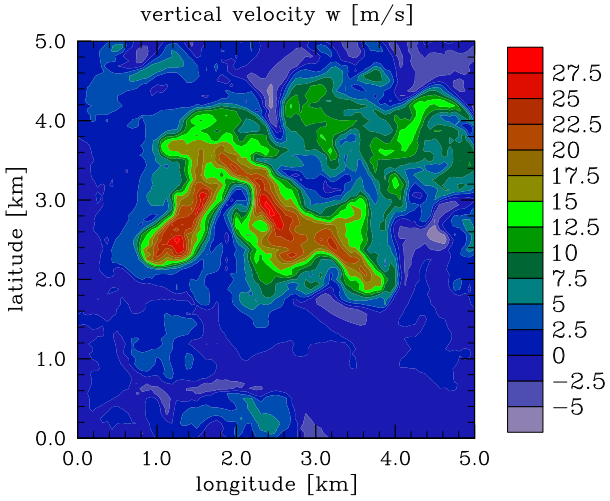

Figure 46: Horizontal slice of the global w_{max} column from the computation with a spatial step size of 62.5 m.

Even if this particular convective tower is quite frayed table 2 proves that the typical values of velocities and dimensions are comparable to those for the towers in the simulation with lower resolution.
In analogy with table 1 concerning the simulation with the 62.5 m step size, table 2 lists the columns around the local maxima of vertical velocity for the simulation with the 125 m step size. The table contains the maximum velocities w_{max}, u_{max}, v_{max}, the height of the maximum vertical velocity $h_{w_{max}}$ and the

t [h : min]	w_{max} [ms^{-1}]	u_{max} [ms^{-1}]	v_{max} [ms^{-1}]	$h_{w_{max}}$ [km]	Δz_{cloud} [km]	Δx_{cloud} [km]	Δy_{cloud} [km]
3 : 00	14.186	8.618	7.683	4.688	4.813	1.313	1.250
3 : 10	17.000	11.853	11.266	5.688	8.250	1.000	1.313
3 : 20	17.478	9.662	10.004	6.125	3.563	1.625	1.125
3 : 30	14.936	10.612	10.073	6.125	4.250	1.188	1.000
3 : 40	15.498	9.602	8.659	3.563	2.375	0.875	0.250
3 : 50	21.415	8.738	10.207	5.000	4.188	0.750	0.875
4 : 00	14.939	10.404	9.581	5.000	3.438	0.688	0.688
4 : 10	19.004	12.099	13.151	6.313	3.625	3.563	1.375
4 : 20	16.975	9.589	8.661	4.313	5.813	1.125	1.313
4 : 30	19.277	10.087	9.640	3.813	4.938	1.750	1.125
4 : 40	20.110	11.647	11.882	4.500	3.938	1.063	1.875
4 : 50	20.652	9.996	10.628	4.313	3.750	2.125	1.625
5 : 00	17.737	13.583	12.593	9.000	6.813	2.563	2.875
5 : 10	21.500	14.584	10.593	6.000	3.875	2.625	1.438
5 : 20	13.568	9.990	11.431	3.563	2.813	1.313	0.813
5 : 30	21.070	11.696	10.527	4.125	4.938	1.000	1.250
5 : 40	29.395	20.148	19.736	7.063	5.938	1.500	3.313
5 : 50	12.741	9.240	8.938	3.563	3.188	1.125	2.625
6 : 00	13.405	7.782	8.420	3.125	2.250	1.500	0.813
Ø	17.941	11.049	10.720	5.046	4.355	1.510	1.418

Table 2: Characteristic velocities and dimensions for the simulation with a spatial step size of 62.5 m.

extensions of the deep convective cloud Δz_{cloud}, Δx_{cloud}, Δy_{cloud}. The last row yields the averaged values of the table's sample.

The sample of table 2 shows somewhat smaller values with respect to the

maximum vertical velocity and the spatial extensions of the cloud compared to the simulation with lower resolution. The characteristic scales and orders of magnitude in the deep convective events, however, do not change with the refinement of the computational grid. This means that the spatial step size of 125 m is probably sufficient for resolving the relevant physical phenomena.

5.4 Simulation with the horizontal Coriolis Parameter

To remind the reader of the role of the different Coriolis Forces, the momentum balances are stated as they are given by Etling [2]:

$$\begin{aligned}
\frac{\partial u}{\partial t} + u\frac{\partial u}{\partial x} + v\frac{\partial u}{\partial y} + w\frac{\partial u}{\partial z} - fv + f^*w &= -\frac{1}{\varrho}\frac{\partial p}{\partial x} \\
\frac{\partial v}{\partial t} + u\frac{\partial v}{\partial x} + v\frac{\partial v}{\partial y} + w\frac{\partial v}{\partial z} + fu &= -\frac{1}{\varrho}\frac{\partial p}{\partial y} \\
\frac{\partial w}{\partial t} + u\frac{\partial w}{\partial x} + v\frac{\partial w}{\partial y} + w\frac{\partial w}{\partial z} - f^*u &= -\frac{1}{\varrho}\frac{\partial p}{\partial z} - g
\end{aligned} \tag{38}$$

In the above equations $f = 2\Omega \sin\phi$ and $f^* = 2\Omega \cos\phi$ represent the vertical and the horizontal Coriolis parameters, respectively, where Ω is the earth's rotation frequency and ϕ is the geographical latitude.

The horizontal Coriolis parameter f^* is usually neglegted in meteorological applications. It is not implemented in the standard version of UCLA-LES1.1 either whereas the vertical Coriolis parameter f is.

A first approach to judge the importance of the Coriolis term involving the horizontal Coriolis parameter and occuring in the horizontal momentum balance for the u-velocity is to look at its order of magnitude. This is done in the same way as for the individual terms of the vertical momentum balance discussed in section 5.2. Based on the output of the reference run the Coriolis term of interest is computed during postprocessing. Figure 47 shows the usual scatter plot over height for the Coriolis term assuming geographical mid latitude.

In figure 48 we plot the distribution over height of the time derivative from the u-equation.
We observe a situation comparable to that of the vertical momentum balance: In the w-equation, the time derivative term is by one order of magnitude larger than the buoyancy term, in the u-equation, the time derivative term is by one order of magnitude larger than the Coriolis term.

For the purpose of performing a simulation with the horizontal Coriolis parameter it is implemented in UCLA-LES1.1. Besides this, we stay with the same setting described in section 3.2. In this way we are able to compare simulation data of the computation without to that with the horizontal Coriolis parameter.

It has to be emphasised that as soon as there are changes in the equations there are changes in the stochastic process of cloud formation. For one fixed system the results are deterministic and reproducible but with a different setting

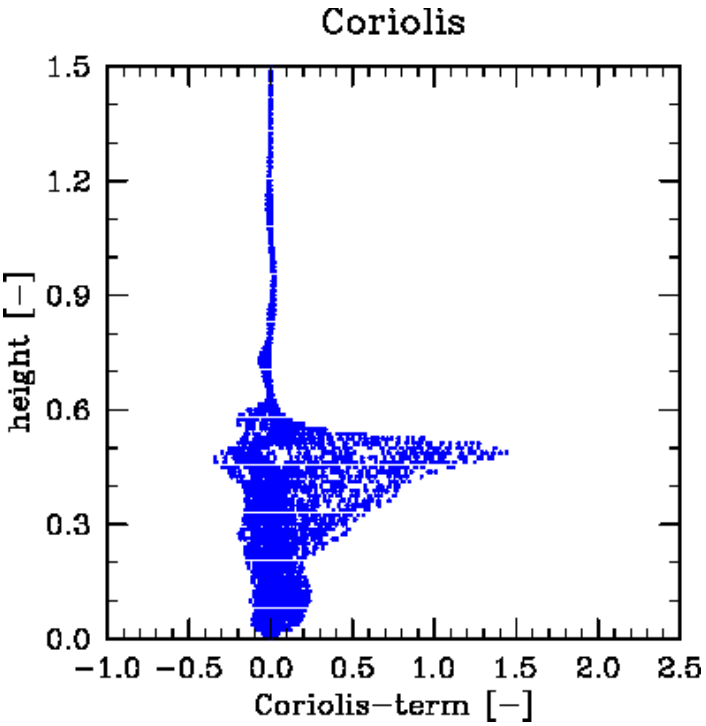

Figure 47: Dimensionless Coriolis term of the u-equation $(w^{(0)}\widehat{\boldsymbol{\Omega}}_{\shortparallel} \times \boldsymbol{k}) = w^{(0)} \cos\phi$.

the same columns as in the usual setting cannot be observed. So there is no direct comparison possible by means of the same tower in time and space for both cases.

We choose the deep convective column forming around the global maximum of vertical velocity, the global w_{max} column, for detailed analysis. In the computation with the horizontal Coriolis parameter the global maximum of vertical velocity amounts to $31.401\,\mathrm{ms}^{-1}$ and is observed after five hours and forty minutes of simulated time (output frequency: 10 min). Figures 49 and 50 show the usual contour plots of w on vertical and horizontal slices through the cloud region, respectively. (For comparison: The contour plots of the global w_{max} column for the standard setting without the horizontal Coriolis parameter are figures 17 and 18).
From these plots we cannot deduce an influence of the inclusion of the horizontal Coriolis parameter on the dynamics of the deep convective column. Also the scatter plot of the accumulated vertical momentum balance in figure 51 does not show considerable differences to figure 43 which is the corresponding plot from the simulation without the horizontal Coriolis parameter.

The reduced asymptotic model suggests the prominent role of the horizontal Cori-

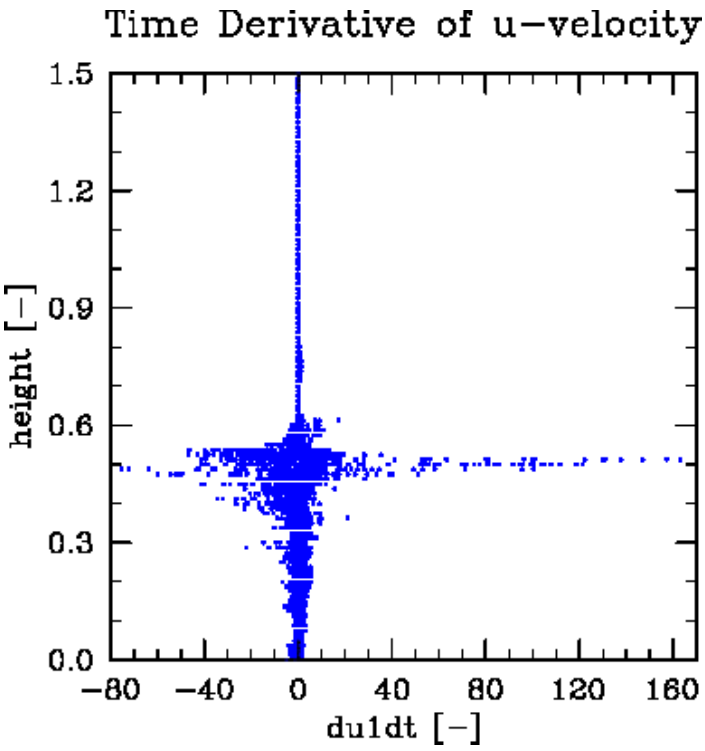

Figure 48: Dimensionless time derivative of the first order u-velocity $u_t^{(1)}$.

olis parameter in the u-equation. As visualisation of the horizontal flow streamlines are plotted for the horizontal cross section through the maximum vertical velocity of the specific cloud. We show two examples from the reference case without the horizontal Coriolis parameter: The column analysed in detail in sections 5.1 and 5.2 (see slices in figures 6 and 8) whose streamlines are displayed in figure 52 and the global w_{max} column of the reference run (see slices in figures 17 and 18) whose streamlines are situated in figure 53. In contrast figure 54 presents the streamlines of the global w_{max} column of the run including the horizontal Coriolis parameter (see slices in figures 49 and 50). The background colour in all three plots indicates the absolute value of horizontal velocities.
There is no difference to observe that could be attributed to the absence or presence of the horizontal Coriolis parameter during the computation.

The horizontal Coriolis parameter acts only on the u-velocity and not on the v-velocity. This suggests that there should be a preferential direction among the components of horizontal velocity in the data of the simulation including the horizontal Coriolis parameter. Such a difference between u and v should not be observable in the data of the simulation without the horizontal Coriolis parameter.

To find out whether this is true, we build averages of the velocity components themselves and their absolute values, respectively, over the deep convective

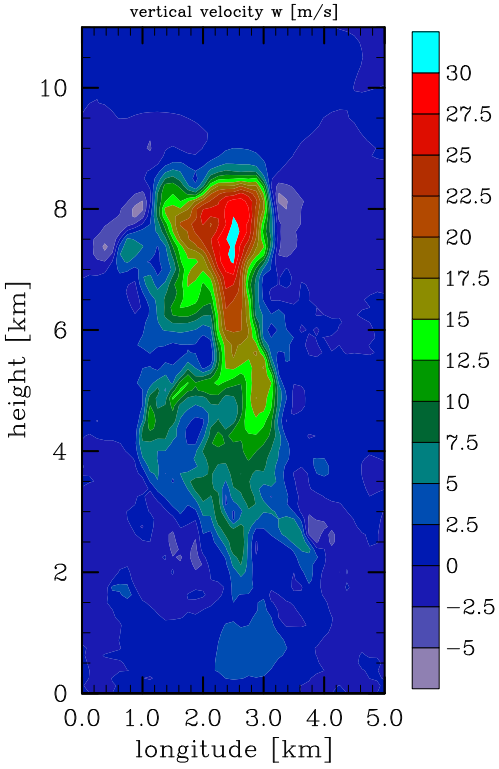

Figure 49: Vertical slice of the global w_{max} column from the computation including the horizontal Coriolis parameter.

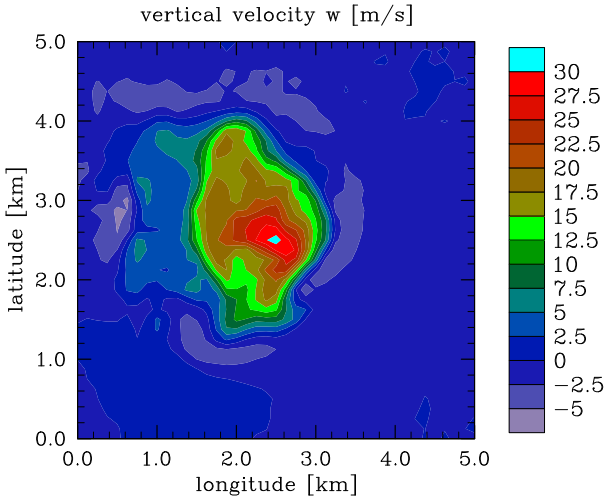

Figure 50: Horizontal slice of the global w_{max} column from the computation including the horizontal Coriolis parameter.

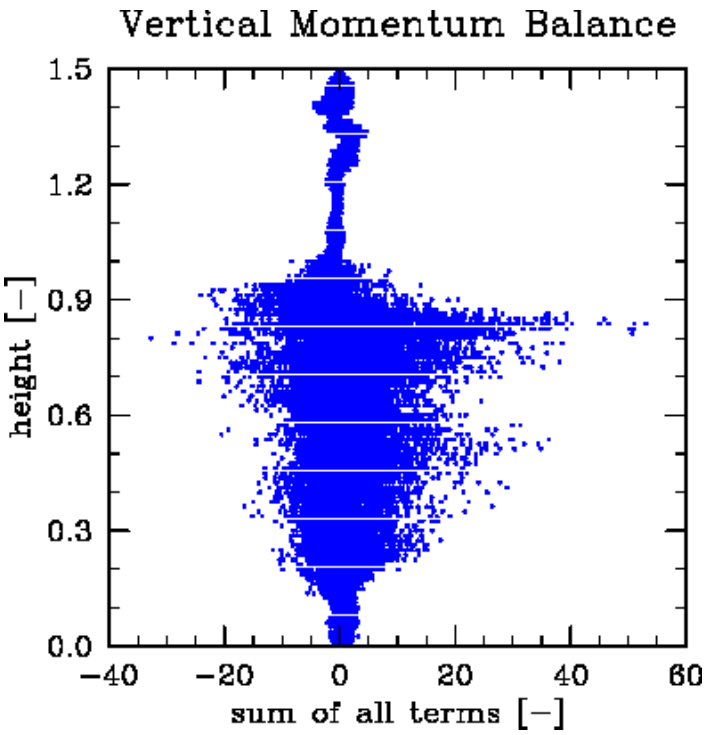

Figure 51: Accumulated vertical momentum balance for the global w_{max} column from the computation including the horizontal Coriolis parameter.

column. This means we add up all the values of the cloud-subdomain and devide by the number of grid points contained in it. This is done for both the simulation without (table 3) and with (table 4) the horizontal Coriolis parameter.
For each point in time the tower around the local maximum of vertical velocity is listed. Both tables provide the maximum velocity in the cloud w_{max}, the averaged velocity components $\overline{w}$, $\overline{u}$, $\overline{v}$, the averaged absolute values of the velocity components $\overline{|w|}$, $\overline{|u|}$, $\overline{|v|}$ and the number of grid points in the cloud. The last row in both tables yields the average values of the table's sample.

There is no preferential direction to detect in the computation with the horizontal Coriolis parameter (in the computation without neither). The difference between u computed without horizontal Coriolis parameter and u computed with horizontal Coriolis parameter is due to the slightly higher velocity level in the sample of the simulation including the horizontal Coriolis parameter.

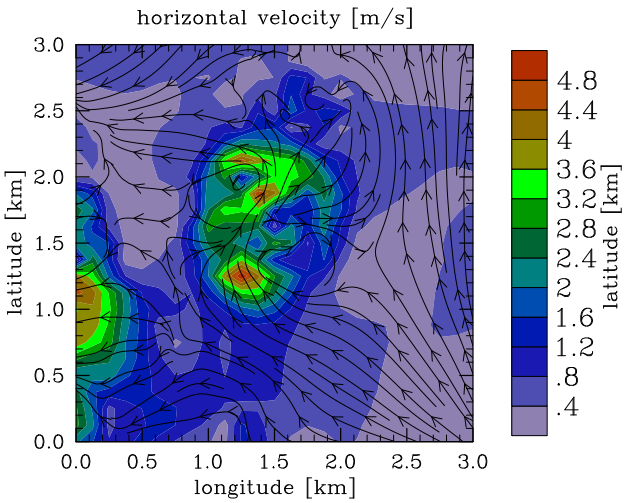

Figure 52: Streamlines and absolute value of horizontal velocities for the column of figures 6 and 8 – computation without horizontal Coriolis parameter.

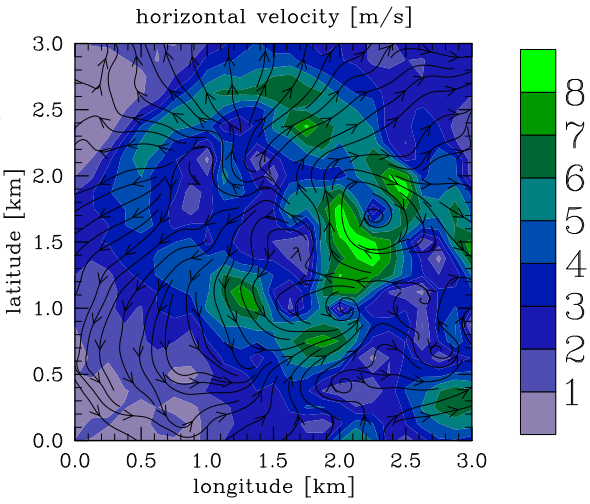

Figure 53: Streamlines and absolute value of horizontal velocities for the column of figures 17 and 18 – computation without horizontal Coriolis parameter.

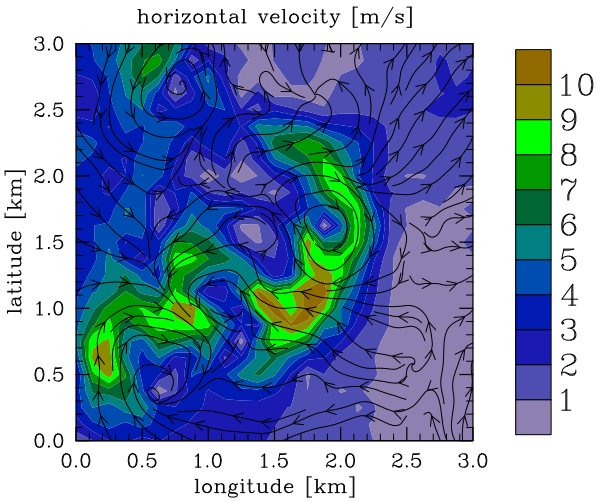

Figure 54: Streamlines and absolute value of horizontal velocities for the column of figures 49 and 50 – computation with horizontal Coriolis parameter.

t [h : min]	w_{max} [ms^{-1}]	$\overline{w}$ [ms^{-1}]	$\overline{\lvert w \rvert}$ [ms^{-1}]	$\overline{u}$ [ms^{-1}]	$\overline{\lvert u \rvert}$ [ms^{-1}]	$\overline{v}$ [ms^{-1}]	$\overline{\lvert v \rvert}$ [ms^{-1}]	# grid points [–]
3 : 00	15.376	0.805	1.084	0.003	0.421	0.008	0.438	3420
3 : 10	19.243	1.630	1.933	−0.065	0.696	0.016	0.765	3861
3 : 20	21.742	1.808	2.520	0.027	1.179	−0.066	1.174	21420
3 : 30	18.778	0.754	1.477	−0.133	0.684	−0.050	0.623	3780
3 : 40	20.493	2.227	2.874	0.044	1.040	−0.200	0.966	3200
3 : 50	20.999	1.462	2.161	−0.122	0.907	−0.014	1.021	3500
4 : 00	20.750	2.459	3.034	−0.024	1.339	0.085	1.347	19040
4 : 10	22.456	2.063	2.665	−0.154	1.178	0.170	1.255	5184
4 : 20	18.842	1.424	2.124	−0.086	1.179	−0.034	1.221	35910
4 : 30	25.624	4.026	4.567	−0.116	2.112	−0.454	2.136	14175
4 : 40	22.735	2.008	2.562	0.177	1.207	−0.055	1.165	10032
4 : 50	30.993	2.615	3.135	0.059	1.592	0.118	1.619	30240
5 : 00	20.323	2.016	2.770	0.074	1.761	−0.252	1.500	19516
5 : 10	21.232	1.957	2.501	−0.270	1.570	0.240	1.685	26448
5 : 20	18.890	2.457	3.403	0.096	2.046	0.091	1.711	3770
5 : 30	26.219	3.124	3.710	0.061	1.917	0.038	1.767	41272
5 : 40	23.254	3.620	4.443	0.240	2.117	0.109	2.447	17472
5 : 50	20.380	3.247	3.686	−0.461	2.122	−0.342	2.384	27144
6 : 00	18.796	2.245	3.030	0.208	1.570	−0.256	1.616	12408
Ø	21.428	2.208	2.825	−0.023	1.402	−0.045	1.413	15883

Table 3: Velocities averaged over the cloud-subdomain – simulation without horizontal Coriolis parameter.

t [h : min]	w_{max} [ms^{-1}]	$\overline{w}$ [ms^{-1}]	$\overline{\lvert w \rvert}$ [ms^{-1}]	$\overline{u}$ [ms^{-1}]	$\overline{\lvert u \rvert}$ [ms^{-1}]	$\overline{v}$ [ms^{-1}]	$\overline{\lvert v \rvert}$ [ms^{-1}]	# grid points [–]
3 : 00	14.435	0.771	1.019	0.003	0.573	0.002	0.539	7020
3 : 10	19.343	1.239	1.517	0.012	0.562	0.057	0.593	4554
3 : 20	19.998	1.234	1.633	−0.019	0.637	0.055	0.591	4700
3 : 30	23.251	2.694	3.183	−0.089	1.424	0.034	1.431	10608
3 : 40	19.955	1.510	2.230	0.107	0.893	0.136	0.915	3200
3 : 50	20.749	2.793	3.434	0.080	1.328	−0.038	1.576	4920
4 : 00	17.628	1.798	2.617	−0.097	1.778	−0.081	1.582	21120
4 : 10	17.936	1.441	1.785	0.108	1.117	−0.057	1.181	6480
4 : 20	22.537	4.125	4.726	−0.276	1.903	0.210	2.614	13860
4 : 30	22.082	1.894	2.861	0.111	1.492	−0.185	1.525	6006
4 : 40	22.241	2.210	2.795	−0.043	1.456	0.278	1.373	9450
4 : 50	20.415	3.002	3.514	0.312	1.846	0.414	2.032	6840
5 : 00	28.610	2.273	2.945	−0.018	1.609	0.043	1.522	41400
5 : 10	27.534	3.805	4.579	0.108	1.898	−0.230	1.832	10208
5 : 20	22.949	3.148	3.814	0.031	2.024	0.033	2.209	34500
5 : 30	21.016	2.802	3.266	−0.037	1.436	−0.225	1.509	8064
5 : 40	31.401	2.207	2.798	−0.023	1.491	−0.080	1.499	51842
5 : 50	29.501	3.892	4.351	0.050	2.190	0.001	2.026	23919
6 : 00	28.141	3.423	3.863	0.220	2.166	0.083	1.814	27600
Ø	22.617	2.435	2.996	0.028	1.464	0.024	1.493	15594

Table 4: Velocities averaged over the cloud-subdomain – simulation with horizontal Coriolis parameter.

6 Conclusions

This work checks the plausibility of the asymptotic column model for deep convective clouds derived by Carqué et al. [1]. For this purpose the physical statements of the reduced model equations are compared to the simulation data of a detailed computational model.

The simulation data confirm the basic assumptions of the asymptotic analysis. The deep convective columns are characterised by a spatially anisotropic structure where the horizontal scale is considerably narrower than the vertical scale. From emergence to breakup the life cycle of one particular deep convective cloud covers a period of about 20 min. The deep convective events are concentrated towers separated from each other.

The main statements of the asymptotically reduced model are approved by the simulation data. The pressure field controls the horizontal flow. The vertical velocity develops freely independent of pressure over the whole depth of the convective cloud. The vertical velocity is directly determined by the buoyancy induced by the potential temperature deviation relative to the background stratification.

The asymptotic perturbation quantities are extracted from the simulation data. Their values in the cloud region are of $\mathcal{O}(1)$.

The sum of the terms in the vertical momentum balance equation computed during postprocessing is considerably smaller than the large time derivative and advection terms themselves.

Refining the spatial step size of the equidistant computational grid from 125 m to 62.5 m does not influence the results in a qualitative sense: Even with the coarser grid the relevant physical phenomena appear to be represented.

Analysing the streamlines reveals no preferential direction among the components of horizontal velocity in the computation with the horizontal Coriolis parameter.

Acknowledgements

This research work is partially funded by Deutsche Forschungsgemeinschaft, Grants KL 611/14 and KL 611/15.

Bibliography

[1] Gunter Carqué, Antony Z. Owinoh, Rupert Klein, and Andrew J. Majda. Asymptotic Scale Analysis of Precipitating Clouds. ZIB-Report 08-03, Konrad-Zuse-Zentrum für Informationstechnik Berlin, January 2008.

[2] Dieter Etling. *Theoretische Meteorologie: Eine Einführung*. Springer-Verlag, Berlin, Heidelberg, New York, Barcelona, Hongkong, London, Mailand, Paris, Tokio, second edition, 2002.

[3] Wojciech W. Grabowski. Coupling Cloud Processes with the Large-Scale Dynamics Using the Cloud-Resolving Convection Parameterization (CRCP). *Journal of the Atmospheric Sciences*, 58(9):978–997, May 2001.

[4] Wojciech W. Grabowski. MJO-like Coherent Structures: Sensitivity Simulations Using the Cloud-Resolving Convection Parameterization (CRCP). *Journal of the Atmospheric Sciences*, 60(6):847–864, March 2003.

[5] Wojciech W. Grabowski. An Improved Framework for Superparameterization. *Journal of the Atmospheric Sciences*, 61(15):1940–1952, August 2004.

[6] Marat F. Khairoutdinov and David A. Randall. A Cloud Resolving Model as a Cloud Parameterization in the NCAR Community Climate System Model: Preliminary Results. *Geophysical Research Letters*, 28(18):3617–3620, 2001.

[7] Marat F. Khairoutdinov, David A. Randall, and Charlotte DeMott. Simulations of the Atmospheric General Circulation Using a Cloud-Resolving Model as a Superparameterization of Physical Processes. *Journal of the Atmospheric Sciences*, 62(7):2136–2154, July 2005.

[8] Randall J. LeVeque. *Numerical Methods for Conservation Laws*. Birkhäuser, Basel, Boston, Berlin, second edition, 1992.

[9] Andrew J. Majda. Multiscale Models with Moisture and Systematic Strategies for Superparameterization. *Journal of the Atmospheric Sciences*, 64(7):2726–2734, 2007.

[10] Andrew J. Majda and Yulong Xing. New Multi-Scale Models on Mesoscales and Squall Lines. *Communications in Mathematical Sciences*, submitted 2008.

[11] David A. Randall, Marat F. Khairoutdinov, Akio Arakawa, and Wojciech W. Grabowski. Breaking the Cloud Parameterization Deadlock. *Bulletin of the American Meteorological Society*, 84(11):1547–1564, November 2003.

[12] Axel Seifert. *Parametrisierung wolkenmikrophysikalischer Prozesse und Simulation konvektiver Mischwolken*. PhD thesis, Universität Karlsruhe (TH), July 2002.

[13] Axel Seifert and Klaus Dieter Beheng. A Double-Moment Parameterization for Simulating Autoconversion, Accretion and Selfcollection. *Atmospheric Research*, 59-60:265–281, 2001.

[14] Bjorn Stevens. *The UCLA-LES: Version 1.1*, August 2007.

[15] URL: `https://wci.llnl.gov/codes/visit/home.html`.

[16] URL: `http://www.mathworks.com/`.

[17] URL: `http://www.ncl.ucar.edu/`.

[18] URL: `http://www.pik-potsdam.de/institute/organization/it-services/userguides/computing/power`.

[19] URL: `http://www.unidata.ucar.edu/software/netcdf/`.

[20] Morris L. Weisman and Joseph B. Klemp. The Dependence of Numerically Simulated Convective Storms on Vertical Wind Shear and Buoyancy. *Monthly Weather Review*, 110(6):504–520, June 1982.